954818

# RESMEDES Spain 1996

## Ground data collection and analysis report

P.J. van Oevelen, M.A.M. Vissers and I.H. Woodhouse

954818

# Contents

# List of Figures

4

# List of Tables

# Chapter 1

# Introduction

## 1.1 General objectives and goals

The Mediterranean area is a geographical region where temporal variability of land-surface processes has shown tendencies towards aridification and desertification. The land degradation observed in this "desertification belt" of the northern hemisphere is a major "global change" problem and as such addressed in the land surface oriented IGBP core projects (Bolle, 1995). The REmote Sensing of the MEediterranean Desertification and Environmental changeS (RESMEDES) project is funded through the EC under contract ENV4-CT95-0094. The project is a continuation of past research efforts in the Mediterranean especially the EFEDA'91 project for which the special observation period was in the summer of 1991 (Bolle & Streckenbach, 1992). The general objective of RESMEDES is *to contribute with remote sensing methods to the understanding of the geographical as well as the temporal variability of land surface processes in the Mediterranean area with special emphasis on an early detection of tendencies towards aridification and desertification* (Bolle, 1995).

For this purpose it deals with the inference from measurements made in space of quantities that are needed;

1. to diagnose the state of the surface;

2. to run models that provide insight to the processes occurring at the surface;

3. to prepare the ground for future quasi-operational inference of information that may be used in prognostic models to simulate scenarios of possible future developments.

Since land degradation and desertification have two main causes, climate change and human impact, the changes to be analysed occur at two different scales. The first one is the large or "synoptic" scale for which climatic influences are the most important. The second one is the regional scale at which the human impact can be of more influence. The synoptic scale is in the project addressed by taking the whole Mediterranean area while the regional scale is tackled by small scale experiments throughout the Mediterranean, but mainly in Barrax, Spain and the Tuscany region in Italy.

The work in the RESMEDES project has the following three aims (Bolle, 1995):

i To compile data sets of land surface quantities that are used in a descriptive way (as "indices") to analyze changes that occur at the land surfaces;

ii to compute with the aid of these data sets and collateral information fluxes in order to study in more detail the process behind the changes;

iii to aggregate the parameters as well as the fluxes into the scale of the models that are operated to study regional climate processes or to develop scenarios of possible future climates.

To be able to assess the "desertification in the Mediterranean" one has to differentiate in space and time: results from studies at specific sites have to be placed in the context of the processes/events that take place in the whole Mediterranean basin. Therefore the goal of the project is to study the degree of desertification-threat around the Mediterranean by analyzing multi-temporal information inferred from observations made in space with respect to:

- the temporal variability of land surface properties, specifically of those needed in models, and;

- of the energy, momentum, and water fluxes between the surface and the atmosphere that are responsible for the coupling between the surface and the atmospheric climate system and are needed to determine energy and water budgets as well as to validate models.

The department of Water Resources will focus on the determination of the vegetation cover and soil water content in the upper layer of the soil by means of active microwave remote sensing.

## 1.2 Soil moisture and vegetation assessment using ERS-1/2 SAR and WSC

### 1.2.1 Objectives of the investigation

SAR is a useful tool in acquiring quantitative data on vegetation cover and soil surface moisture content (Dubois et al., 1995). The all-weather capability of microwave systems makes the ERS-1/2 SAR a suitable instrument to monitor vegetation development and soil moisture dynamics at different scales. Especially the WSC-data with a spatial resolution of approximately 50 km (cross track) and a global coverage within 3 to 4 days seems to have great potential for studies over large areas (Wismann et al., 1996). Even though cloud cover in the Mediterranean is not severe, SAR has some major advantages over optical systems: there is no need to correct for local atmospheric conditions (haze, dust), and the monitoring capability does not stop in rainy periods, which may be of particular interest.

The radar backscatter level as measured by ERS-1/2 (available as PRI or precision images) over land surfaces is primarily a function of the soil surface moisture content, soil surface roughness and the amount and structure of the vegetation cover (Ulaby et al., 1986) . The main objective of this study is the mapping and monitoring of vegetation and surface soil moisture by means of radar remote sensing. This should lead (in combination with other investigations within the framework of RESMEDES) to assessment of desertification indicators and to the monitoring of desertification in the Mediterranean (Bolle, 1995).

This study focuses in particular on the combined use of the various ERS-1/2 types of SAR data, namely; interferometry, windscatterometer (WSC) data and precision image (PRI) SAR data.

## 1.2.2   Methodology

The approach to be developed and validated consists of two parts namely data collection/fieldwork and analysis. The analysis can also be subdivided into two steps. The first step is to derive the areal extent of vegetation and its biophysical characterization. For the whole Mediterranean the low resolution windscatterometer data and, for selected subsites, the high resolution PRI and SLC data will be employed. The second step is to estimate soil moisture using an inverted backscatter model such as the INVIEM model (van Oevelen & Hoekman, 1998; van Oevelen & Hoekman, 1994) based upon the forward solution of the Integral Equation Method (IEM) model (Fung et al., 1992; Fung, 1994). However, these models are valid for bare soil conditions and thus in case of vegetation cover the effect of vegetation has to be corrected. This correction will be based upon the University of Texas at Arlington (UTA) radiative transfer model (Karam et al., 1992). A priori knowledge of vegetation extent, and type and of soil physical properties is useful and will be collected through field trips and co-operation with other groups participating in the RESMEDES project.

## 1.2.3   Anticipated results

It is proposed to develop and validate a generally applicable and all-weather methodology to monitor soil moisture and vegetation development at test sites representative for desertification threatened areas in the Mediterranean. The approach is based on SAR observations. The usefulness of backscatter models to derive soil moisture and to correct for vegetation is investigated and the applicability of interferometric SAR products such as phase and coherency maps will be assessed. The wind scatterometer data will yield clear insights into the temporal and spatial dynamics of these parameters for the whole Mediterranean area at meso-scale. As such the SAR and wind scatterometer observations are complementary.

# 1.3   Outline

This report summarizes the field work performed at the Barrax area in Spain and gives the preliminary results of the analysis obtained sofar. Where the authors feel it necessary additional data from the 1991 EFEDA experiment has been added. The fieldwork is performed as a supporting task to enhance, simplify and verify the analysis of ERS-1/2 microwave data. The high resolution data from ERS-1/2 SAR and derived products such as interferograms have the main focus. The support of low resolution data such as the ERS-Windscatterometer is not specifically addressed. All the data mentioned in this report cannot be used without explicit written permission by the authors. Regardless of wether it data concerns from the authors or other sources.

# Chapter 2

# Site Description

## 2.1 Location

The main site for ground truth data collection is the Barrax area in the Castilla-La Mancha area in Spain. More specifically this site is situated in the western part of the province of Albacete, 28 km from the capital town with the same name. The approximate center coordinates are 39°2'N and 2°10'W. This area was selected for its flatness and the presence of large uniform land-use units, thus minimizing the complications introduced by topographic structures and highly variably roughness. The slopes that can be found in this area are no higher than 2 m. In Figure 2.1 the approximate study area is indicated. Within the Barrax area the ITAP experimental farm of the University of Albacete was the center of the ground truth collection campaign.

## 2.2 Climate

The climate is of the mediterranean type, with heaviest rainfall in spring and autumn and lowest in summer; it presents, so a high grade of continentality, with quite sudden changes from cold months to warm months and high thermic oscillations between the maximum and minimum daily temperatures in all seasons. The average annual temperature is 14.1°C. The hottest month is July with and average temperature of 24.6 °C and the coldest month is January with an average temperature of 3.9 °C. The yearly average maximum temperature is 21.1°C and the minimum temperature is 7.1°C with the absolute extremes being 42.8 °C and -18 °C. The average period of frost goes from the middle of November to the middle of April. The first date frost has ever been recorded is 27th of October, the last date the 2nd of May. The average rainfall is 474m with 72 rainy days. The evapotranspiration according to the method by Thornthwaite is 775mm/yr., being higher than the pluviometer from the month of April to the month of October. According to Papadakis, the climate is "Warm Mediterranean", with a "Cool Oats" winter, a "Rice" type summer, thermic regime "Warm Temperate" and humidity regime "Dry Mediterranean".

## 2.3 Soils

The soils of the area are poorly developed and present a profile type. they belong to the order of *Inceptisols* of the Soil Taxonomy (ref??). taking into account the humidity regime *xerico* of the soils, the subgroups present are the "*Xerochrepts*

Figure 2.1: The approximate location of the study area within Spain.

*Calcixerollics"* or *"Xerochrepts" "Calcixerollix-Petrocalcics"*. They are soils with a superficial horizon *"ochric"* and as subsuperficial horizons of diagnostic, the horizons *"calcic"* and/or *"petrocalcic"*

The main limitations by the soils imposed upon the productivity capacity are the real depth which is small in the area, due to the presence of the petrocalcic horizon with large amounts of total and/or active limestone. The stoniness is in many cases excessive due to the presence on the surface of remains of the petrocalcic horizon. The textures are, in general, quite balanced, with the open-clay predominating, whereas there aren't usually structural problems due to the stabilizing effect of the ion calcium on the structure.

The chemical properties are not usually too unfavorable, although the lack of organic matter and the prolonged cultivating, have contributed to decreasing content of nutritious elements for the plants. The pH oscillates between 7.5 and 8.2 and the contents of limestone are between 30% and 60%. The soils are poor in phosphorus and relatively rich in potassium.

# Chapter 3

# Ground data collection

## 3.1 Land surface cover inventory

At this stage only a land surface cover inventory has been made for the ITAP farm area. This inventory has been made between May 22 until May 25 of 1996. Shown in Figure 3.1 are the various crops, roads, pivot irrigation circles and various other structures. Clearly a large part of the area, about 1/3, can be considerd bare soil, furthermore a considerable part of the area has been planted with barley.

In a later stage a more extensive land cover map is planned either using when available optical data (SPOT or LANDSAT-TM) or microwave data (ERS-1/2 SAR).

## 3.2 Soil moisture measurements

### 3.2.1 Equipment and calibration

The soil moisture data is collected over a depth of about 6 cm using a Time Domain Reflectometry (TDR) system. The system used was the TRIME P2 system consisting of a probe with two parallel rods of 10 cm length connected with a coax cable to the main module which has a digital display giving the volumetric soil moisture content. The rods of the probe are fully inserted into the ground under an angle of 45° with ground resulting in a measurement of the average volumetric soil moisture content over a depth of approximately 6 cm. For a detailed discussion about TDR the reader is referred to Heimovaara and Bouten (1990) and Dasberg and Dalton (1985) .

The soil moisture data is collected along parallel transects on the days ERS-1 and ERS-2 had their overpasses. In Figure 3.2 the transects are indicated for both days.

In Table 3.1 the averages per field of the TDR soil moisture measurements are given.

| Field | 1 | 2 | 3 |
|-------|-----|-----|-----|
| 24/5/96 | 0.064 | 0.145 | 0.094 |
| 25/5/96 | 0.048 | 0.173 | - |

Table 3.1: Field averaged soil moisture content from TDR measurements over 6 cm depth. Fields are indicated in Figure 3.2

Map of ITAP near BARRAX

| | Bare |
| | Beets |
| | Rapeseed |
| | Barley |
| | Alfalfa with rapeseec |
| | Alfalfa |
| | Leek |
| | Peas |
| | Wheat |
| | Orchard |
| | Buildings |
| | Reservoir |

roads
pivot irrigation circles
fields/crop boundaries
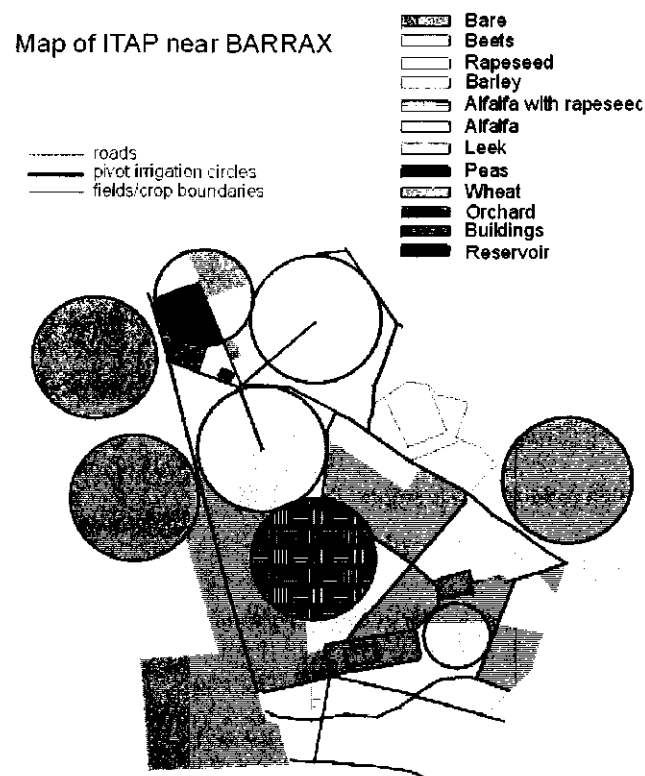
Figure 3.1: A map of the ITAP experimental farm with the crop cover of the fields valid for the end of May 1996 indicated.

**TDR measurements**
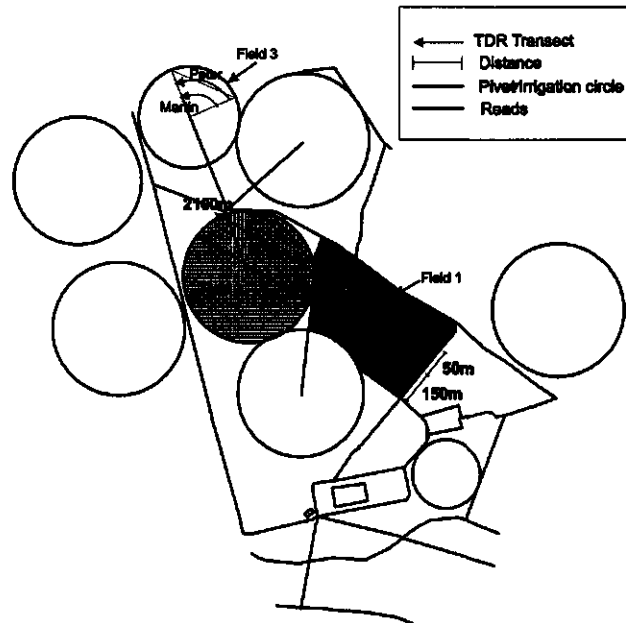


Figure 3.2: The location of the TDR transects within the ITAP experimental farm.

## 3.3  Surface roughness measurements

### 3.3.1  Methods and material

The soil surface roughness, an important quantity in microwave remote sensing modelling, is determined using a needle board (see Fig 3.3). The needle board consists of two aligned areas with different density of needles by which the measurements can be made. Macro roughness can be measured with low density sampling (1 needle per cm) and micro roughness can be measured with high density sampling (3 needles per cm). Each measurement gives 151 samples in both high and low density, where the high density is measured over 50 cm and the low density over 150 cm (Vissers & Hoekman, 1991). The needle board has to be placed level over the surface, the needles can then be lowered such that the top of the needles just hit the surface and altogether give a profile of the soil surface. Of the whole board a photograph is taken and the profile can then be digitised. In this way two sets of $x, z$ coordinates is given for each pair of needles, where "$x$" stands for the distance between the needles and "$z$" is the height of the needles.

The number of measurements made is limited to those surfaces that were distinct and representative for the area. For each measurement location two pairs of measurements are made, resulting in one perpendicular to the row direction (the "$y$" direction) and one parallel to it (the "$x$" direction). Since we assume that the physical processes that cause surface roughness are uncorrelated for both directions, measurements restricted to these two directions are sufficient.

There are several ways to express the surface roughness. In this report we take the root mean square (RMS) (mm) of the height differences, $\sigma$, of the needles, and the autocorrelationlength (cm), $l$, as a measure of surface roughness. With
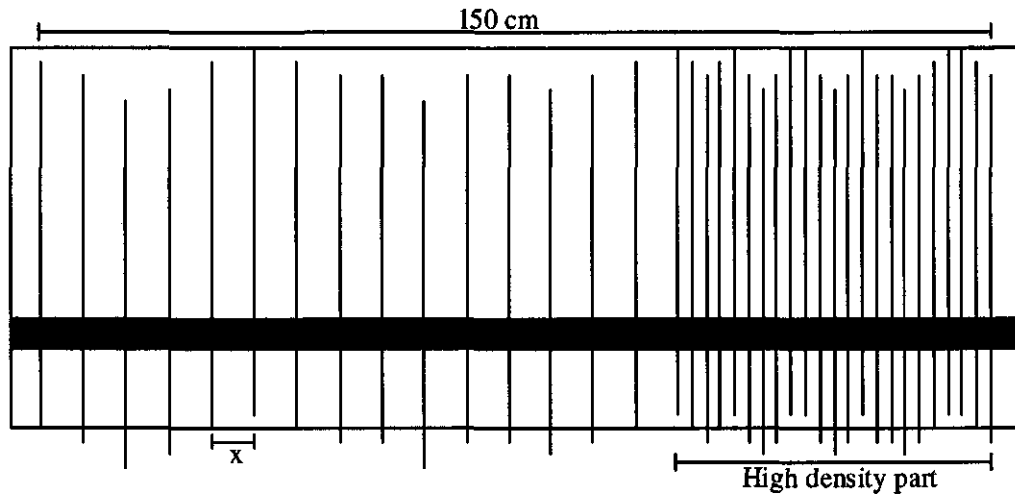
Figure 3.3: Soil profile meter or "needle board"

these values the power density spectrum using the fast fourier Transform (FFT), and the Autocorrelation function using an inverse FFT can be calculated using the algorithms from Press et al. (1992) .

Estimations of root mean square height or $\sigma$ can be determined directly from samples of $h(\mathbf{x})$ and $h(\mathbf{y})$, yielding $\sigma_y$ and $\sigma_x$. Likewise estimations of the autocorrelation functions $C(\mathbf{x})$ and $C(\mathbf{y})$, in $\mathbf{x}$- and $\mathbf{y}$-directions respectively, follow. Because of the assumed independence between the two directions, $C(\mathbf{r}) = C(\mathbf{x})C(\mathbf{y})$. The autocorrelation lengths $l_x$ and $l_y$ are defined as the distance at which the normalised autocorrelation functions (for which $C(0) = 1$) fall off to a value of $1/e$.

The power spectral density function (or power spectrum) is usually defined as the Fourier transform of the unnormalised autocorrelation function:

$$W(\overline{k}) = \frac{\sigma^2}{(2\pi)^2} \int\limits_{-\infty}^{\infty} C(\mathbf{r}) \exp(i\overline{k}r)dr$$

and is also called the surface roughness spectrum. Here $\overline{k}$ is the spatial wave number of the surface ($k = 2\frac{\pi}{\lambda}$), which in this case is related to the electromagnetic wave number $k$ by the expression:

$$\overline{k} = 2k\sin\theta_i$$

Also from the power spectral density (PSD) function the autocorrelation lengths $l_x$ and $l_y$ can be derived from the points where the normalised PSD function falls off to the value $1/e$ as $l_{x,y} = \frac{2}{k_{x,y}}$. Using the theorems of Wiener-Khintchine and Parseval (Press et al., 1992) it can easily be shown that the total area under the power spectrum gives the variance, or 'power' of the surface:

$$\int\limits_{-\infty}^{\infty} W(\overline{k})d\overline{k} = \sigma^2$$

The theory of wave scattering from rough surfaces often assumes that surface autocorrelation functions are Gaussian and may be given as:

$$C(\mathbf{r}) = \exp\left(\frac{-\mathbf{r}^2}{l^2}\right)$$

Then, the surface roughness spectrum $W(\bar{k})$ follows as:

$$W\left(\bar{k}\right) = \frac{\sigma^2 l^2}{4\pi} \exp\left(\frac{\bar{k}^2 l^2}{4}\right)$$

or in the direction of the wave:

$$W\left(2k\sin\theta_i, 0\right) = \frac{\sigma^2 l^2}{4\pi} \exp\left(\bar{k}^2 l^2 \sin^2\theta_i\right)$$

The power spectral density describes both the spread of heights about the mean plane and the height variation along the surface.

Alternative forms of the correlation function can also be given. In general, the exponential form seems to fit measured surface roughness data better. The exponential correlation function can be written as:

$$C(\mathbf{r}) = \exp\left(\frac{-|\mathbf{r}|}{l}\right)$$

For higher order surface properties, such as surface gradients, this function poses problems because of the dicontinuity at the origin. The surface spectrum for the exponential function becomes:

$$W\left(\bar{k}\right) = \frac{\sigma^2}{l^2\pi^2} \frac{1}{\left(\frac{1}{l^2} + \bar{k}^2\right)}$$

Various other correlation function have been suggested. Furthermore it should be noted that surfaces may be described by more than one correlation function. This can be the case, for instance, for surface whith roughness caused by different types of processes. More detailed information on surface roughness descriptions can be found in Ogilvy (1990).

### 3.3.2   Surface roughness data

The surface roughness data is collected on the days prior to the ERS-1/2 overpasses, namely between the 22 and 24 of May, 1996. Special emphasis is put on characteristic roughness features of this region such as pivot irrigation tracks (Figures 3.4 and 3.5).

That these tracks are important is shown on data from the HAPEX-EFEDA 1991 experiment held in the same area. From the data of a multifrequency polarimetric radar, namely the JPL-AIRSAR with C-, L- and P-band and a spatial resolution of about 12m, the effects became very clear (Figure 3.6). Especially in L-, and P-band are the effects clearly visible. However, these effects are not visible in C-band (i.e. same band as ERS-1/2), probably due to the fact that the 5 cm wavelength of this band is too small. In other words the small scale surface roughness of the track is more important in C-band (Figure 3.7).
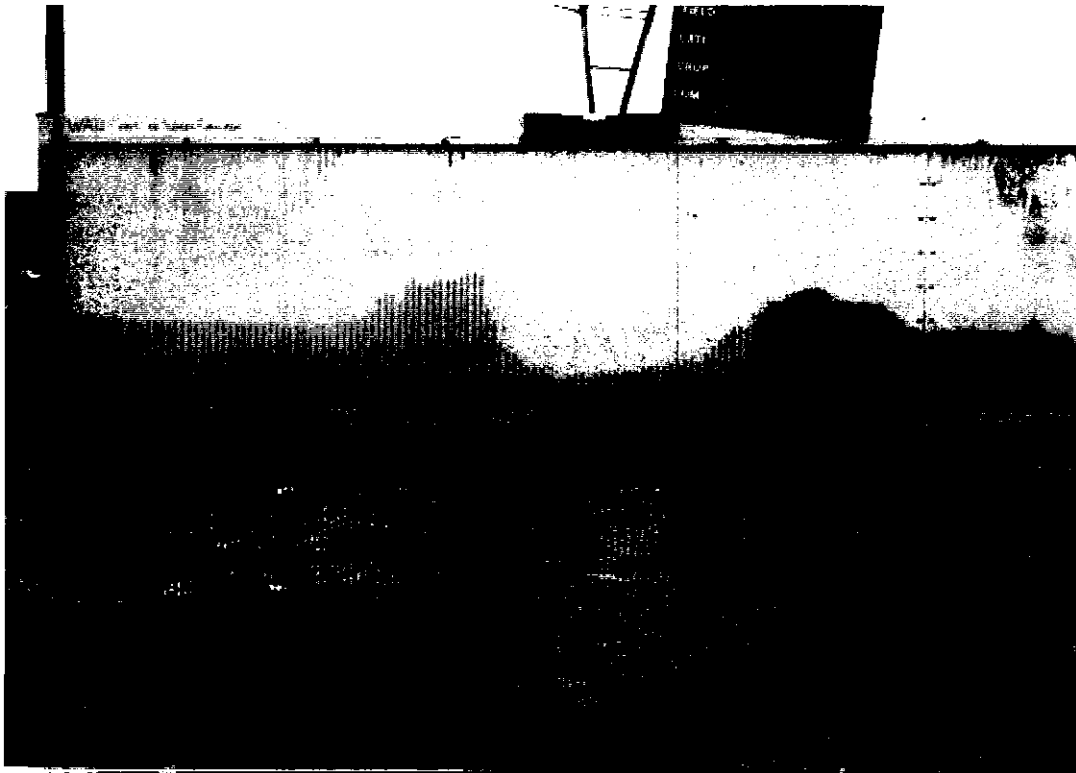
Figure 3.4: Photo showing the pivot irrigation wheel track.

## 3.4 Location determination

### 3.4.1 GPS Measurements

To determine the location in the field at the ITAP experimental farm a global positioning system (GPS, magellan 2000) was used. In Figure 3.8 the measurement locations are indicated. In Table 3.2 the corresponding values of the points in Figure 3.8 are given.

| Point | Latitude | Longitude | UTM (zone =31) | |
|---|---|---|---|---|
| A | 39°02′53″ | 2°06′26″ | 422742.49 E | 4322280.57 N |
| B | 39°02′86″ | 2°05′36″ | 421550.72 E | 4323309.66 N |
| C | 39°03′10″ | 2°05′05″ | 420800.67 E | 4322823.91 N |
| D | 39°03′11″ | 2°05′46″ | 421786.48 E | 4322844.88 N |
| E | 39°03′46″ | 2°05′71″ | 422398.04 E | 4323917.83 N |
| F | 39°04′00″ | 2°05′99″ | 423075.19 E | 4324342.78 N |
| G | 39°03′72″ | 2°05′82″ | 422670.28 E | 4324716.70 N |
| H | 39°03′96″ | 2°05′48″ | 421860.59 E | 4325464.60 N |
| I | 39°03′63″ | 2°05′38″ | 421610.16 E | 4324449.74 N |
| J | 39°03′36″ | 2°04′80″ | 421169.25 E | 4323621.76 N |
| K | 39°03′22″ | 2°04′53″ | 420515.97 E | 4323196.73 N |
| L | 39°02′65″ | 2°04′74″ | 421015.45 E | 4322667.61 N |
| M | 39°02′59″ | 2°04′87″ | 421326.09 E | 4322479.52 N |
| N | 39°01′89″ | 2°05′23″ | 421220.68 E | 4321555.71 N |

Table 3.2: The GPS measurement points given in Latitude/Longitude and UTM co-ordinates.
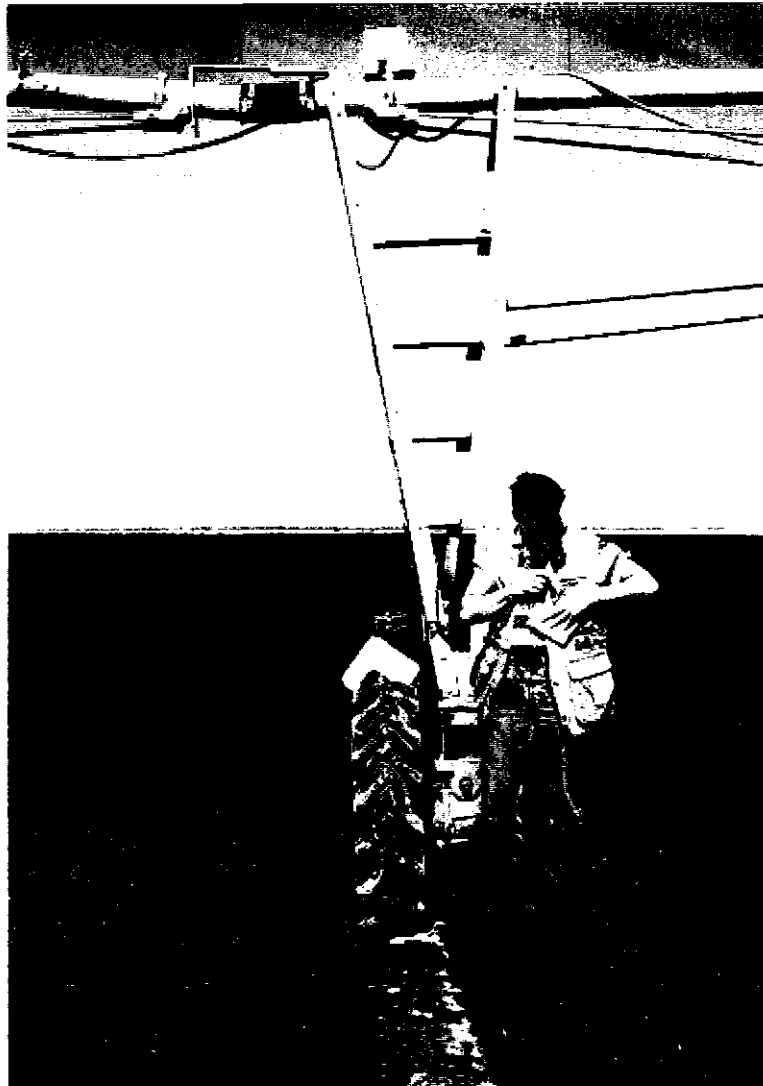
Figure 3.5: Photo showing the tire that causes the wheel tracks in the pivot irrigation fields. A side effect is that the soil becomes compact inside the tracks and after rainfall or irrigation standing water can be present for a while.

Figure 3.6: A total power image of JPL-AIRSAR (June '91, Barrax area around ITAP), with C-, L- and P-band in Red, Green and Blue respectively.



Figure 3.7: JPL-AIRSAR data (June'91, Barrax area around the ITAP center) with from left to right C-, L- and P-band respectively. Clearly the effects of the pivot irrigation can be seen as also the tracks of the tires within the irrigation fields.

**GPS Locations**
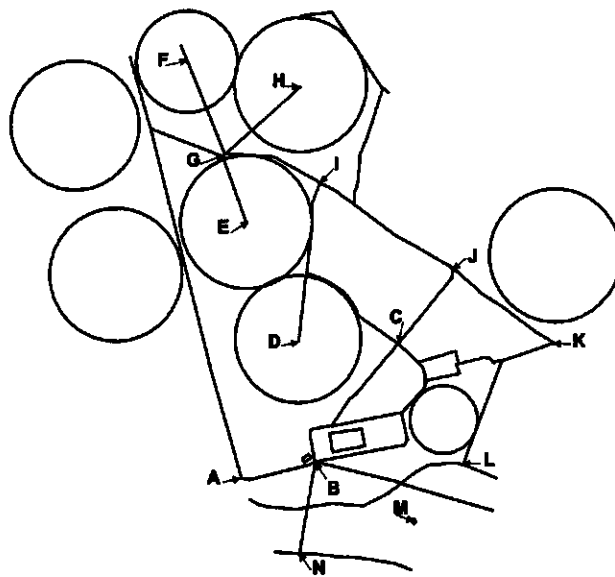


Figure 3.8: The GPS measurement locations at the ITAP experimental farm.

# Chapter 4

# Remote sensing measurements

## 4.1 Spaceborne SAR data

### 4.1.1 ERS-1/2 SAR

The ERS satellites (ERS-1 and ERS-2) have a Sun-synchronous, near polar, quasi-circular orbit with a mean altitude of 785 km and an inclination of 98.5°. Most missions will be performed in a 35-day repeat cycle. On board the ERS satellite is the Active Microwave Instrument (AMI) which has several different modes. Two modes are of interest in this study namely, the image mode which will be referred to as ERS-1 SAR and the windscatterometer mode

The ERS-1/2 SAR is a single frequency and polarization radar operating at C-band (5.3 GHz) and VV-polarization. The spatial resolution of the instrument is approximately 25 m and the data are delivered with a pixel size of 12.5 m. The look angle of the instrument at the center of the swath is 23°. The width of the swath is approximately 100 km. In Table 4.1 a summarization is given of the available precision image (PRI) and single look complex (SLC) data (For the latter see paragraph 4.2.3).

| Satellite | Type | Date | Frame | Orbit | Asc./Desc. |
|-----------|------|------|-------|-------|------------|
| ERS-1 | SLC | 24-05-96 | 0783 | 25411 | D |
| ERS-2 | SLC | 25-05-96 | 0783 | 05738 | D |
| ERS-2 | SLC | 04-06-96 | 2813 | 05874 | A |
| ERS-2 | SLC | 13-08-96 | 2813 | 06876 | A |
| ERS-2 | SLC | 22-10-96 | 2813 | 07878 | A |
| ERS-1 | PRI | 24-05-96 | 0783 | 25411 | D |
| ERS-2 | PRI | 25-05-96 | 0783 | 05738 | D |
| ERS-2 | PRI | 04-06-96 | 2813 | 05874 | A |
| ERS-2 | PRI | 13-08-96 | 2813 | 06876 | A |
| ERS-2 | PRI | 22-10-96 | 2813 | 07878 | A |

Table 4.1: Summarization of the available ERS-1 and ERS-2 PRI and SLC data.
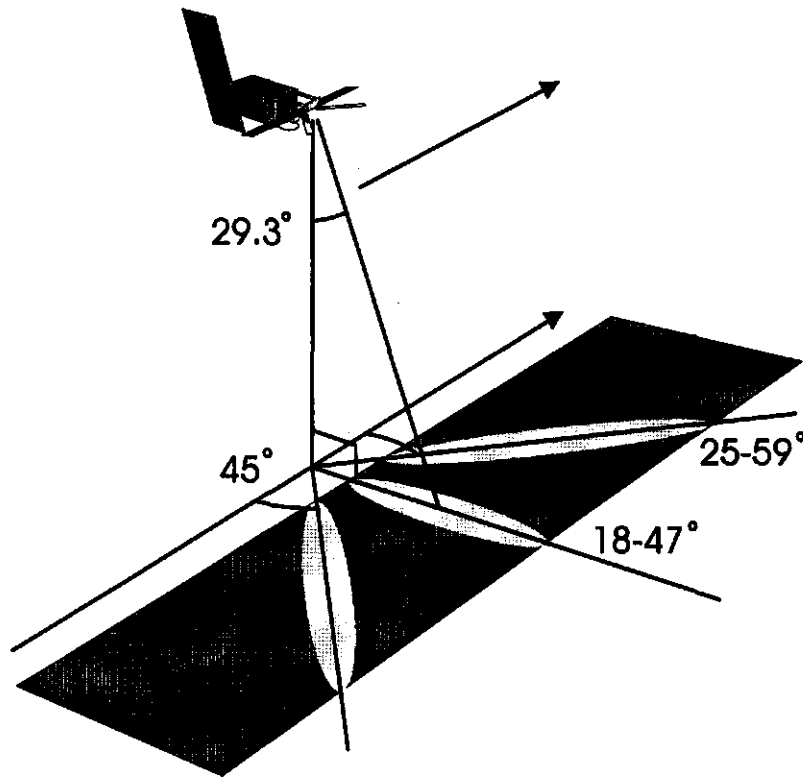
Figure 4.1: Geometry of the ERS Windscatterometer instrument.

## 4.1.2 ERS-1 WSC

The ERS-1 Wind scatterometer (WSC) was designed to obtain information on wind speed and direction over the sea surface. It operates by measuring the variation in the radar reflectivity of the sea as a function of look angle due to the presence of small ripples made by the wind close to the water surface. The instrument consists of 3 antennas producing 3 beams looking 45° forward, sideways and 45° backwards with respect to the satellite's flight direction (see Figure ??). These beams continuously illuminate a 500 km wide swath as the satellite moves along its orbit. Across the swath local incidence angles range from 18-47° for the midbeam and 25-59° for the forward and aft beams, and 19 measurements are made across the swath. Thus three backscatter measurements at each grid point are obtained at different viewing angles and separated by a short time delay. These triplets are then used routinely to extract wind speed and direction over sea surfaces through the use of mathematical models. Measurements are also made over land surfaces and these triplets can therefore be used to retrieve surface parameters over land.

The Wind Scatterometer has a spatial resolution of the order of 45 km along and across track with a radiometric stability of <0.57 dB, and a localization accuracy of better than 5 km. The operating frequency is 5.3 GHz with vertical transmit and receive (VV) polarization.

The Wind Scatterometer is mounted on the ESA ERS-1 platform. The satellite has a near circular, polar, sun synchronous orbit with an inclination of 98.52 degrees and altitude of 782 to 785 km. The ERS-SAR and the wind Scatterometer cannot operate simultaneously.

## 4.2 Image data processing

### 4.2.1 ERS PRI data

The ERS precision image data that has been obtained is given in Table 4.1. These data are multi-look (3) data with 16 bits per pixel. The pixel size is 12.5 m in ground range and 12.5 m in azimuth. One full scene is 100 km in ground range and at least 102.5 km in azimuth. The data are converted to normalized radar cross section $\sigma^o$ expressed in dB. the data is delivered in ground range.

### 4.2.2 ERS WSC data

Windscatterometer data from the ERS-1/2 satellites has been obtained for five global regions, for the period August 1991 to October 1995 and are available on two CD-ROMs. The filename convention is as follows:

EYYMMDD.KKK

where YY, MM, DD is the year, month and day, respectively and KKK the code for the area as can be delineated from Table 4.2. This table also illustrates the coordinates of the five regions, and the periods of data coverage. In this report, only data from the Scandinavian region are considered.

| Site Coordinates | File Ending | latmax | latmin | lonmax | lonmin | |
|---|---|---|---|---|---|---|
| Scandinavia | sca | 70 N | 55 N | 35 E | 10 E | [Apr. 95 - Oct. 95][+] |
| | | | | | | [Aug. 91 - Mar. 95][*] |
| Sahel | sah | 20 N | 7 S | 17 E | 3 W | [Apr. 95 - Oct. 95][+] |
| | | | | | | [Aug. 91 - Mar. 95][*] |
| Kalimantan | kal | 8 N | 5 S | 120 E | 106 E | [Apr. 95 - Oct. 95][+] |
| | | | | | | [Aug. 91 - Mar. 95][*] |
| Mediterranean | med | 48 N | 26 N | 40 E | 10 W | [Apr. 95 - Oct. 95][+] |
| | | | | | | [Aug. 91 - Mar. 95][*] |
| Amazon | ama | 15 N | 10 S | 50 W | 80 W | [Apr. 95 - Oct. 95][+] |

[*] Data for February, 1992 has not been reprocessed yet and is therefore missing.
[+] These data are only for temporary use, they will eventually be updated.

Table 4.2: Available WSC data of the five regions at the Department of Water Resources.

The data is in the form of unformatted binary files consisting of records of 20 integer (2 byte) values that include the date, location, and normalized radar cross section ($\sigma^o$) for the three beams. Incidence and azimuth angles for the three beams are also given.

Full coverage is possible within 4 days, but it should be noted that this may be different during the ice phases, and during periods of extensive SAR imaging.

### 4.2.3 ERS SLC data

The format of single look complex (SLC) data is 16 bit (for both Real and Imaginary part). The number of looks is one (1) and the spatial resolution is less than 10 m in both slant range and azimuth direction. At the Department of Water Resources 5 quarter scenes are available for the Barrax area (Table 4.1).

The SLC data have been processed by the Physics and Electronics Laboratory of TNO (FEL-TNO) to produce phase, correlation and intensity images. The output data is in slant range, with the pixels averaged over 3 pixels in slant direction and

15 in azimuth direction. The spatial resolution of the data in slant range is about 8 m (cf. approx. 20 m in ground range) and 4 m in azimuth direction. Therefore the data have almost square pixels.

# Chapter 5

# Data analysis and preliminary results

## 5.1   Soil moisture estimation using ERS- SAR

Microwave remote sensing of soil moisture is based upon the large sensitivity of the dielectric properties of a soil to its moisture content. The dielectric properties largely influence the interaction between soil and microwave radiation. Two different types of microwave systems are used: (1) passive microwave systems that measure the microwave emissivity of the earth's surface being most sensitive to soil moisture content, vegetation moisture content and physical temperature, (2) active microwave systems that measure the microwave backscatter coefficient being most sensitive to soil moisture content, vegetation moisture content, surface roughness and the structure of vegetation. Passive microwave remote sensing of soil moisture is generally most straightforward because the vegetation effects can be regarded as a simple attenuation of the microwave signal (van Oevelen & Hoekman, 1998). The use of SAR data for soil moisture estimation is more complex, mainly due to the strong non-linear effects of roughness and vegetation.

Various algorithms, both physically based and empirical, are available for soil moisture estimation by means of SAR (Chauhan, 1995; Chen et al., 1995; Engman & Chauhan, 1995). Most models are empirical of nature and thus their applicability is usually limited .Van Oevelen and Hoekman (1994) have developed the INVIEM model (van Oevelen & Hoekman, 1998) a numerical inversion based upon the forward solution of the Integral Equation Method (IEM) model (Fung et al., 1992; Fung, 1994). The IEM model is a physically based model with a large range of validity and is revised to incorporate volume scattering effects (Fung et al., 1996). Dubois *et al.*, 1995 developed a semi-empirical model calibrated with data sets from ground based radar experiments. The latter has been applied to various data sets and seems to work rather well (Ji et al., 1996). However, these models, as are most of the soil moisture retrieval algorithms, are only valid for bare soil conditions and thus in case of vegetation cover the effect of vegetation has to be corrected. This correction can for example be based upon -simplified- radiative transfer modelling, such as the University of Texas at Arlington (UTA) model (Karam et al., 1992). A priori knowledge of vegetation extent, and type and of soil physical properties is therefore extremely useful.

In Figures 5.1 to 5.4 are the comparisons shown for the TDR measurements versus the ERS soil moisture estimates. Along with the statistics give in Table 5.1 several conclusions can be drawn. The INVIEM model which has not been fine tuned, i.e. the roughness classes given as input were a cross section for the whole

Figure 5.1: Soil moisture estimates of ERS-1/2 compared with TDR soil moisture measurements of top 5 cm. of soil. Low 'l' and high 'h' estimates refer to the lower and upper boundaries of the soil moisture estimate range. Points 1 to 63 refer to the bare soil field (not irrigated) and points 64 to 93 refer to the irrigated corn field.

area not specifically these two fields, gives for the bare soil field reasonable results. For the corn field which was irrigated the differences between measured data and estimated data are considerable. Clearly the effect of irrigation is present resulting in higher soil moisture estimates but they considerably overestimate the measured values. A reason for this discrepancy can be in the fact that TDR measurement times did not coincide with the overpass times of both ERS-1 and ERS-2. The TDR measurements were taken in the morning while the overpasses were at 10.23 pm in the evening. Another explanation can be that the vegetation amount was already to high to be neglected. However, this can only be verified with polarimetric radar data which is not available. Using C-band radar at the spatial and radiometric resolutions of ERS are not ideal for soil moisture estimation. For bare fields the estimates are in good agreement but for vegetated fields (even with low vegetation cover) the influence on the backscatter at C-band is too significant to be ignored in the modeling. A good correction algorithm is still not available to correct for these vegetation effects because the description of the plant structure, which is very important, is too complex to describe in simple models such as the Cloud model (Attema & Ulaby, 1978).

The next step in research will be to investigate the effect of roughness on soil moisture determination by comparing data from EFEDA'91 with the data collected under this RESMEDES project. After the effect of surface roughness has been determined for this area it will be feasible to better explore the temporal and spatial variation of soil moisture using ERS data without ground truth verification.

## 5.2  Land surface parameters retrieval using ERS-WSC data

The dynamic nature of land surfaces has long been neglected in climate modeling, due mainly to the lack of sufficient or adequate data. Global optical observation

Figure 5.2: Soil moisture estimates of ERS-1/2 compared with TDR soil moisture measurements of top 5 cm. of soil. Low 'l' and high 'h' estimates refer to the lower and upper boundaries of the soil moisture estimate range. Points 1 to 63 refer to the bare soil field (not irrigated) and points 64 to 93 refer to the irrigated corn field.

data, such as those provided by AVHRR on board the NOAA series of satellites, have not been able to supply some of the most crucial information required by climate modelers. A simple, mixed target model has been developed for extracting geophysical products out of ERS-Windscatterometer data. Such sub-pixel level inversion technique is possible using scatterometer data, thanks to their high radiometric accuracy and range of measurement incidence angles. The method enables observations of geophysical components having different time-constants within a resolution pixel.

The ERS-1 Wind Scatterometer (WSC) instrument, was designed to measure the near-surface wind field over the ocean by inferring the wind speed and direction from measurements of the surface radar backscatter. Measurements are also made, however, over land and several studies have highlighted the relationship between the low resolution scatterometer data and surface geophysical parameters such as vegetation cover, surface roughness and surface soil moisture content. Figure 5.5, for instance, shows the strong correlation between NDVI and percentage vegetation cover as derived from the ERS-Windscatterometer over a test region in the Sahel. While the nominal ground resolution of the data is coarse ( 45 km) the ability to provide global coverage within 4 days, regardless of local weather conditions or solar illumination, makes the WSC instrument ideally suited for meso-scale monitoring of global land surface characteristics.

**Mixed Vegetation and Bare Surface Backscatter Model** The backscattered signal from a scatterometer measurement cell may consist of contributions from a number of surface features. These include volume scattering from various types of vegetation of changing density, and surface scattering from a variety of bare soil types and rock surfaces. Features such as open water and man-made structures, when present, will also contribute. For the present study, the resolution cell is represented by an equivalent surface consisting of a combination of only two surface types: dense, homogeneous vegetation (pure volume scattering) with a fractional surface area denoted by $C$, and bare soil with effective (homogeneous) roughness
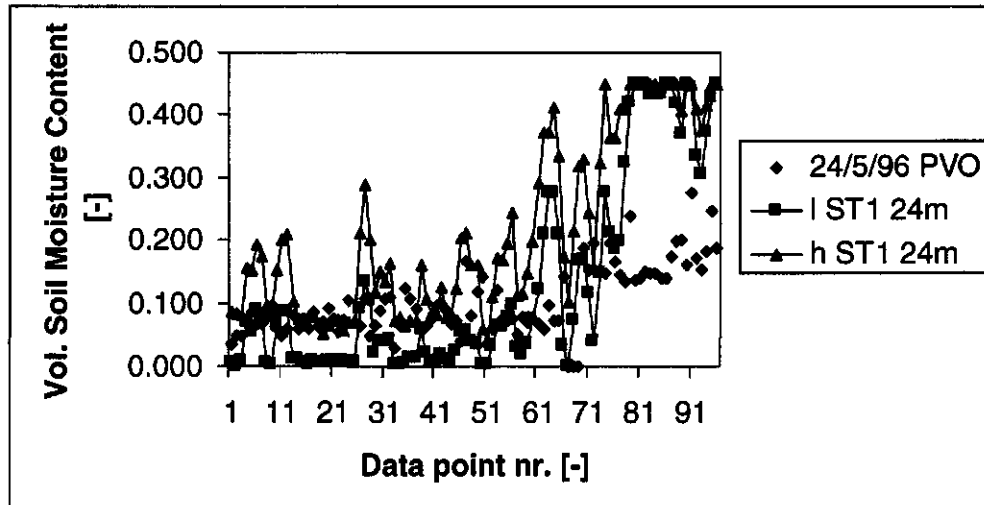
Figure 5.3: Soil moisture estimates of ERS-1/2 compared with TDR soil moisture measurements of top 5 cm. of soil. Low 'l' and high 'h' estimates refer to the lower and upper boundaries of the soil moisture estimate range. Points 1 to 63 refer to the bare soil field (not irrigated) and points 64 to 93 refer to the irrigated corn field.

and dielectric properties (surface scattering). The total backscatter is therefore considered to be an incoherent sum of three backscattering mechanisms: these are (vegetation) volume scattering, surface scattering from the bare soil layer, and specular (double-bounce) reflection between the trunk and ground. In addition, a fourth term may be added which accounts for all other contributions not included in the first three. Since this term may include contributions from such features as highly specular surfaces, its overall effect may be considered to be a random term on the forward model.

Mathematically, the total backscattering cross-section $\sigma^0$ consists of a linear sum of those four contributions:

$$\sigma^0\left(\theta_{\text{inc}}\right) = C\sigma^0_{\text{cover}}\left(\theta_{\text{inc}}\right) + (1-C)C\sigma^0_{\text{bare}}\left(\theta_{\text{inc}}\right) + \sigma^0_{\text{double}}\left(\theta_{\text{inc}}\right) + \sigma^0_{\text{others}}\left(\theta_{\text{inc}}\right) \tag{5.1}$$

where,

$\theta_{\text{inc}}$ : local incidence angle,

$C$ : equivalent fractional vegetation cover,

$\sigma^0_{\text{cover}}$ : contribution from equivalent vegetation cover (volume scattering with $\frac{\sigma^0_{\text{cover}}}{\cos\theta_{\text{inc}}}$ = const ), and with,

$$\sigma^0_{\text{bare}}\left(\theta_{\text{inc}}\right) = \frac{|R_g|^2}{2s^2\cos^4\theta_{\text{inc}}}\exp-\tan^2\left(\frac{\theta_{\text{inc}}}{2s^2}\right) \tag{5.2}$$

where,

$R_g$: Fresnel reflection coefficient at normal incidence,

$s$ : RMS slope of the surface roughness, and with,

$$\sigma^0_{\text{double}}\left(\theta_{\text{inc}}\right) = TR_1R_2\sin^2\left(\theta_{\text{inc}}+45°\right) \tag{5.3}$$
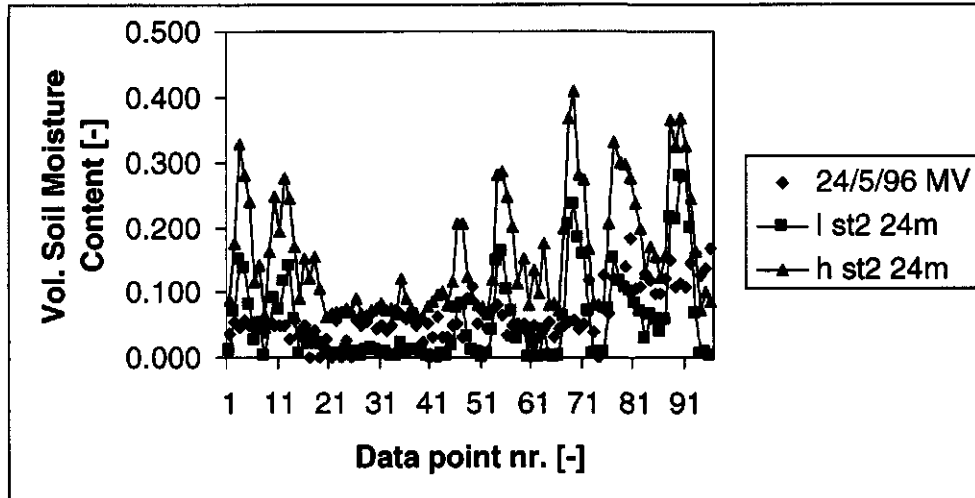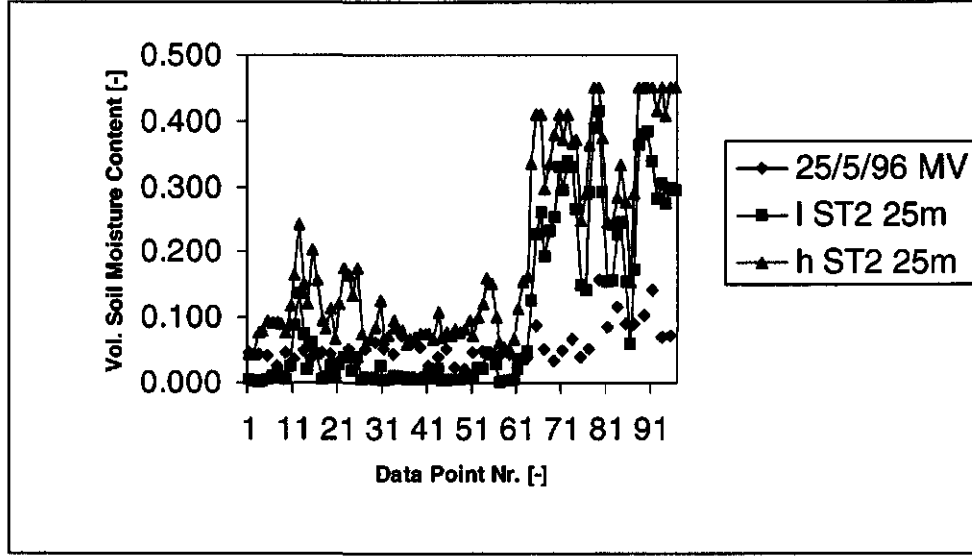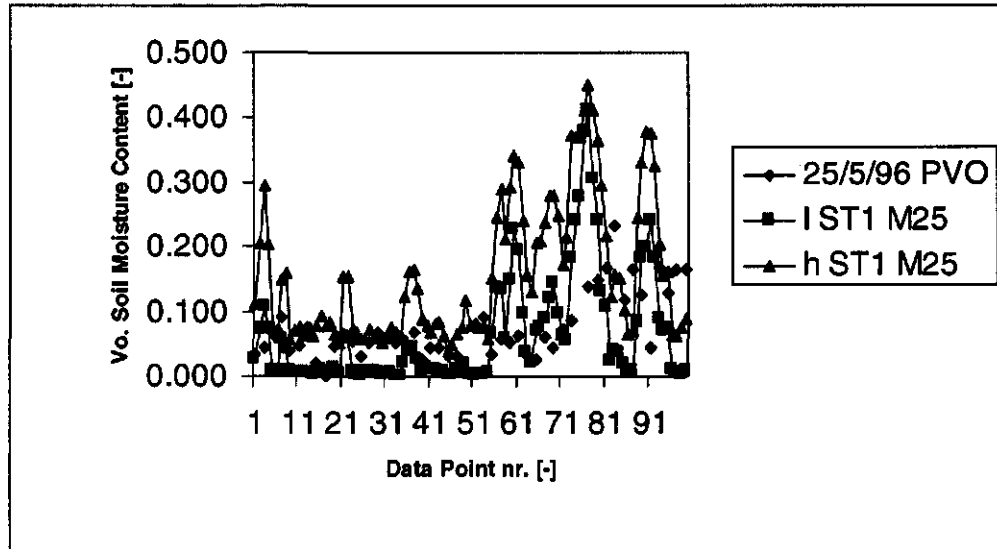
Figure 5.4: Soil moisture estimates of ERS-1/2 compared with TDR soil moisture measurements of top 5 cm. of soil. Low 'l' and high 'h' estimates refer to the lower and upper boundaries of the soil moisture estimate range. Points 1 to 63 refer to the bare soil field (not irrigated) and points 64 to 93 refer to the irrigated corn field.

where,

    $T$        : scaling factor,

    $R_1$       : Fresnel reflection coefficient of the local ground,

    $R_2$       : Fresnel reflection coefficient of the trunk.

This model contains a maximum of 8 unknowns. With the assumption of mixed targets, no dependence on the azimuth look-angle has been foreseen, i.e., no predominant terrain slope within a resolution cell is precluded in the model. Simplifying assumptions are made in the present study to reduce the number of unknowns:

1. $\sigma^0_{cover}$ has been tuned to the respective geographical locations under investigation based on existing data;

2. both $R_1$ and $R_2$ have been estimated assuming a complex dielectric constant of $\varepsilon = 10 - j$;

3. $\sigma^0_{others}$ represents a random term (noise), hence not subject to inversion.

The remaining 4 unknowns are constrained during the inversion process as follows:

- $0 \leq C \leq 1$, where $C = 1$ corresponds to a 100 % vegetation cover;

- $0 \leq |Rg| \leq 1$, where a high value of $|Rg|$ corresponds to a high soil moisture content;

- $0 \leq s$, where a higher value represents a high surface roughness;

- $0 \leq T$, the double bounce term which allows the existence of a local maximum of NRCS around 45° incidence angle.

|         | Field | No. points | Mean Meas. | Mean Est. low | Mean Est. high | RMSE low | RMSE high |
|---------|-------|------------|------------|---------------|----------------|----------|-----------|
| 24-May  |       |            |            |               |                |          |           |
| ST1     | Bare  | 64         | 0.077      | 0.047         | 0.141          | 0.062    | 0.077     |
|         | Corn  | 29         | 0.155      | 0.315         | 0.386          | 0.180    | 0.242     |
| ST2     | Bare  | 64         | 0.046      | 0.034         | 0.126          | 0.039    | 0.085     |
|         | Corn  | 29         | 0.106      | 0.105         | 0.220          | 0.083    | 0.133     |
| 25-May  |       |            |            |               |                |          |           |
| ST1     | Bare  | 32         | 0.050      | 0.032         | 0.118          | 0.044    | 0.072     |
|         | Corn  | 15         | 0.121      | 0.136         | 0.253          | 0.100    | 0.145     |
| ST2     | Bare  | 32         | 0.045      | 0.028         | 0.113          | 0.035    | 0.069     |
|         | Corn  | 15         | 0.081      | 0.267         | 0.363          | 0.182    | 0.276     |

Table 5.1: Comparison of Soil moisture measurements (TDR) over top 5cm and soil moisture estimates of ERS-1 and ERS-2 in May 1996. Given are the mean and root means square errors of the measurement and estimates. Low and High refer to the lower and upper boundary of the soil moisture estimates range.

## 5.2.1 Parameter Inversions over RESMEDES Test Sites

Initial investigations have shown that the retrieval algorithm when applied to the Mediterranean region exhibits general trends in the vegetation cover that one would expect for the area. The seasonal variations were also qualitatively as expected. However in order to investigate further the applicability of this model for monitoring vegetation dynamics in the Mediterranean area it is necessary to apply it to smaller areas which can be quantitatively compared with data from other sources.

Figure 5.6 displays the quantitative retrieval results for effective vegetation cover and surface reflectivity for a (1 degree wide) line of longitude (2.2°W coinciding with the Barrax site) over a period of 4 years. Each column of this diagram represents a retrieval from one month's worth of WSC data, and extends in latitude from 26°-48°N. This line crosses the Bay of Biscay between 43° and 47°N, and the Mediterranean between 35° and 37°N, which explains the very low retrieved vegetation cover and high reflectivity in these regions.

In the retrieved vegetation cover the seasonal periodicity is quite clear, with summer growth in Southern Spain and in the grasslands of Morocco (≈32°N). The extent and duration of this growth clearly varies between different years indicating the potential for using such data as a means of long term monitoring of vegetation dynamics in the Mediterranean area.

Although these data contain features that one would expect for the area, they have yet to be compared with ancillary data, such as NDVI, for the same locations and time periods. Such a comparison will also be made with retrievals for localized areas (11) coinciding with the RESMEDES test sites. Two examples of such retrievals are shown in Figure 5.7 and Figure 5.8, for the Barrax and Tuscany areas respectively. These figures show retrieved vegetation cover and reflectivity, over the five year period. Unfortunately, due mostly to the increased use of the ERS-SAR in these regions, the data coverage is relatively poor. Proper assessment of these data will require comparison with NDVI or local meteorological data.
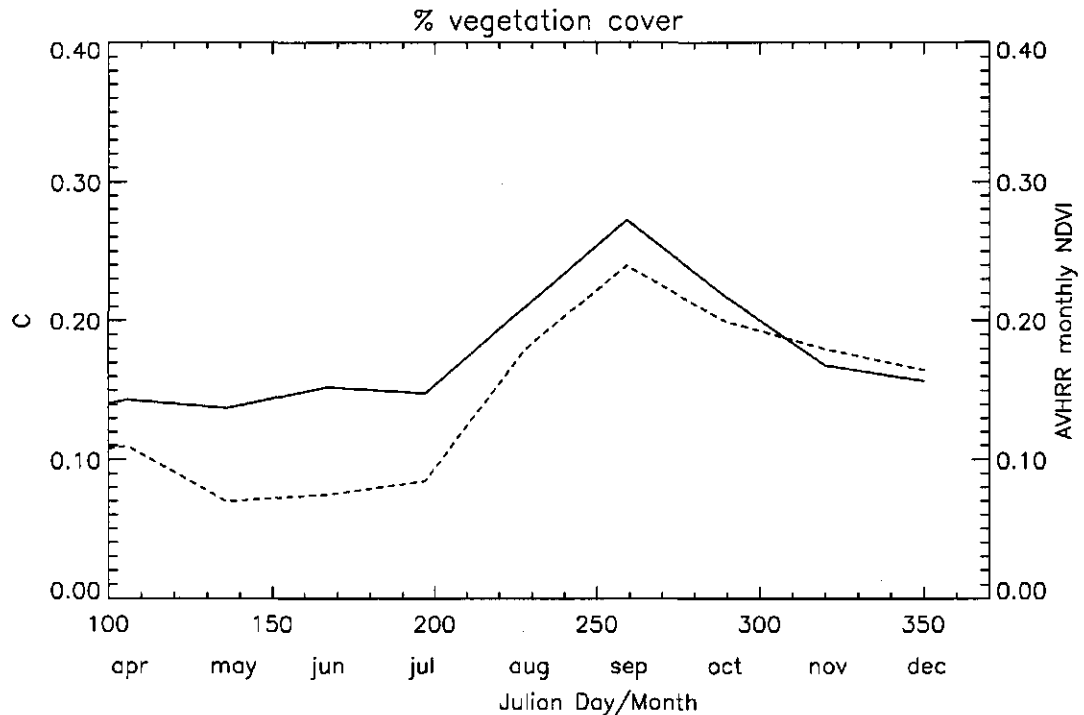
Figure 5.5: Correlation of NDVI and Windscatterometer retrieved vegetation cover for a site in the African Sahel.

## 5.3 Analysis of ERS- SLC data

### 5.3.1 Interferometry

The single look complex (SLC) data of ERS-1 can be used for a technique called multi-pass interferometry. Interferometry is a technique based on relating the signals from two spatially separated antennas illuminating the same area. The distance between the antennas is called the *baseline*. The same approach can also be taken using one antenna and relating the signals from the repeat passes over the same site ((Zebker et al., 1994)). Although in the latter case the antennas do not illuminate the same area at the same time, if the ground is completely undisturbed between the two viewings the two sets of signals will be highly correlated and a spatial baseline may be established. The performance of a radar interferometer system depends on instrument parameters, orbit parameters, data processing errors and post-processing errors. Temporal decorrelation is the most important and often limiting error source for repeat-pass implementation ( (Zebker et al., 1994)). The most important application is the derivation of height information or *digital elevation models* (DEM).

The theory for (multi-pass) interferometry to derive height information can be illustrated using Figure 5.9. Given are two antennas A1 and A2, surface topography given by $z(y)$, the spacecraft altitude by $h$ above a tangent plane at the point of interest, the baseline distance $B$, the range to a point on the ground $r$, the look angle $\theta$,and the angle of the baseline with respect to horizontal $\alpha$ ((Zebker et al., 1994)). Two radar signals transmitted from each antenna and received at the point of transmission will, when properly resampled and cross-multiplied, form an *interferogram* where the phase at each point is proportional to the difference
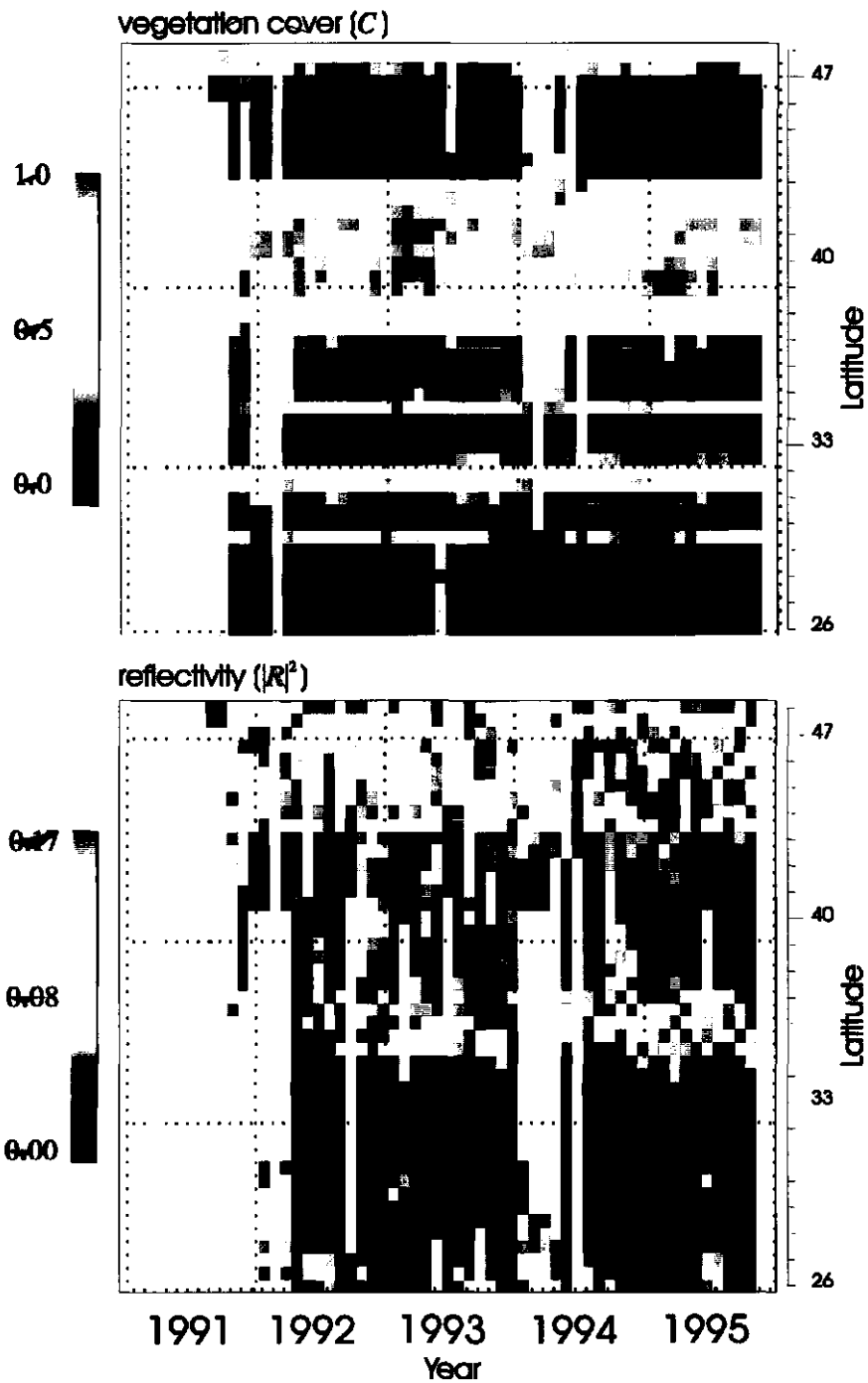
Figure 5.6: Hoevmuller diagrams showing the retrieval results for effective vegetation cover and surface reflectivity for a (1 degree wide) line of longitude centered on 2.2 W coinciding with the Barrax site.
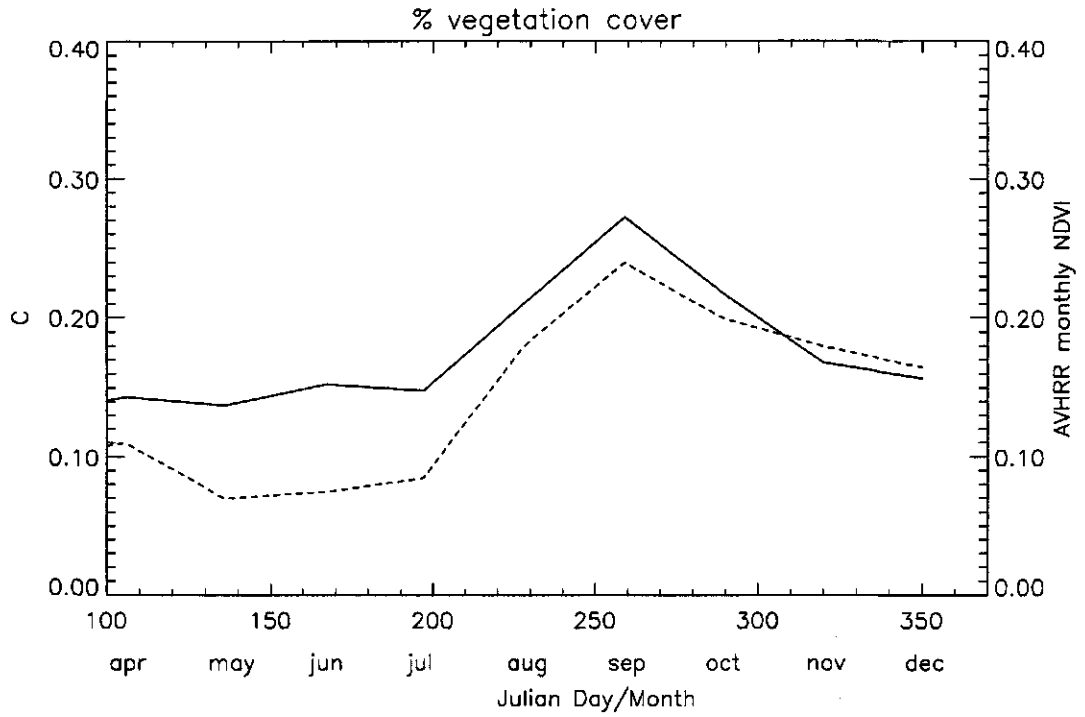
Figure 5.7: Retrieved reflectivity (solid line) and effective vegetation cover (dashed line) for the Barrax site.
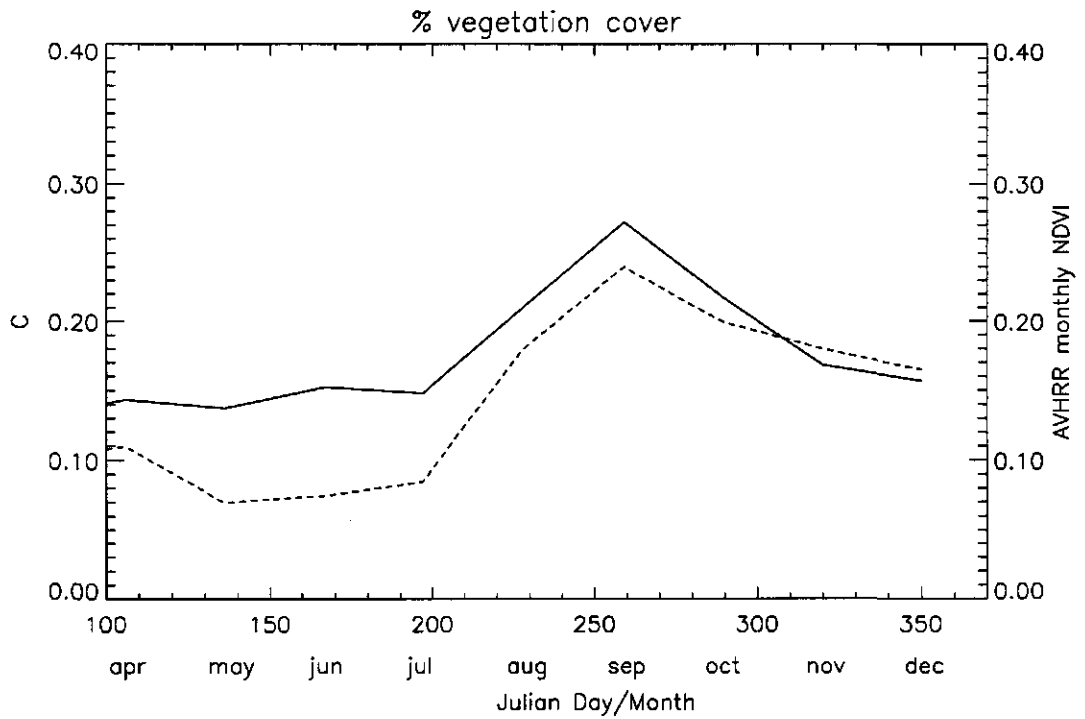


Figure 5.8: Retrieved reflectivity (solid line) and effective vegetation cover (dashed line) for the Tuscany site.
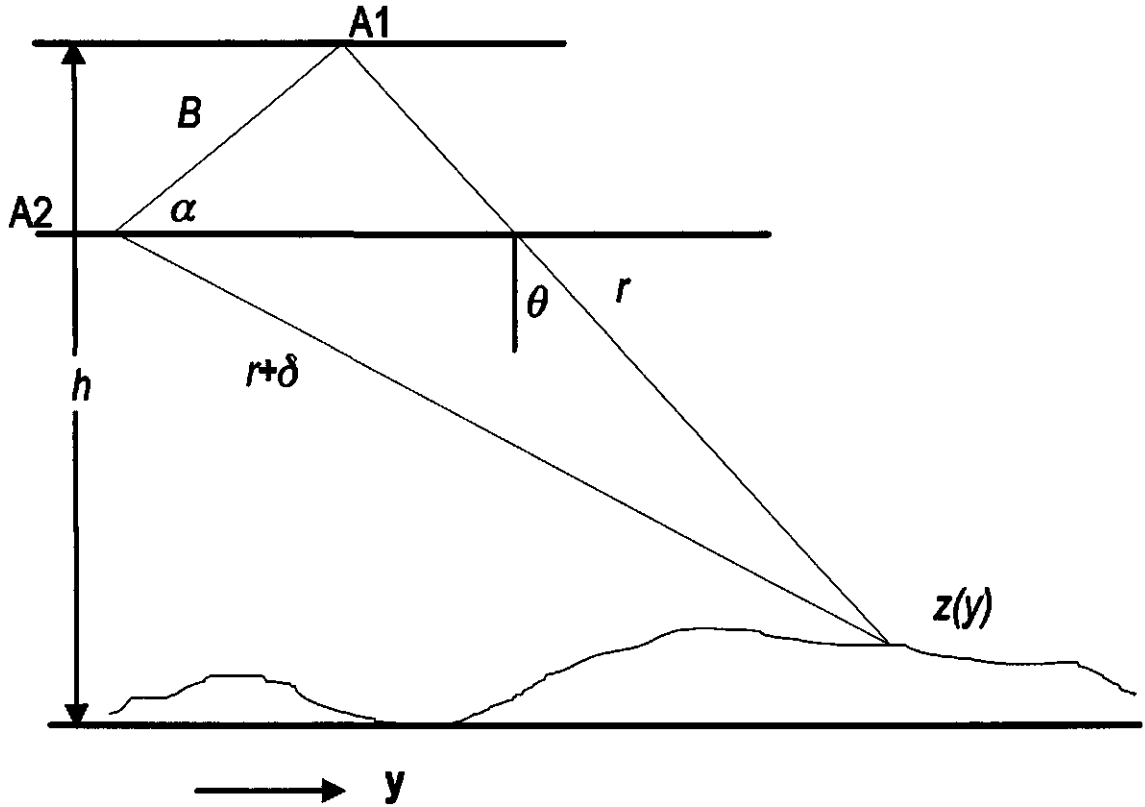
Figure 5.9: Schematic representation of antenna position and relevant parameters for interferometric analysis, adapted from Fig. 1. ( (Zebker et al., 1994))

in path lengths $2\pi$ with the constant of proportionality $\frac{2\pi}{\lambda}$. The following equations can be derived for height as a function of these parameters:

$$\delta = \frac{\lambda\phi}{4\pi} \tag{5.4}$$

$$\sin(\theta - \alpha) = \frac{(r - \delta)^2 - r^2 - B^2}{2rB} \tag{5.5}$$

$$z(r, \theta_{\mathrm{inc}}) = h - r\cos\theta \tag{5.6}$$

where $\phi$ is the measured phase and $\lambda$ is the wavelength.

Two type of errors in the determination of an topographic map are *phase errors* and *attitude errors*. Differentiation of to with respect to yields the error in height estimate as a function of the error in phase estimate to first order:

$$\sigma_z = r\sin\theta\frac{d\theta_{\mathrm{inc}}}{d\phi}\sigma_\phi \approx r\sin\theta_{\mathrm{inc}}\frac{\lambda}{4\pi B\cos(\theta_{\mathrm{inc}} - \alpha)}\sigma_\phi$$

$$\sigma_z = \frac{\lambda r}{4\pi B}\left[\sin\alpha - \cos\alpha\tan(\alpha - \theta_{\mathrm{inc}})\right]\sigma_\phi \tag{5.7}$$

where $\sigma_z$ and $\sigma_\phi$ are the deviations of height and phase respectively; i.e. $\frac{\sigma_z}{\sigma_\phi} \approx \frac{dz}{d\phi}$. The attitude errors result from errors in knowledge of the baseline alignment, i.e.
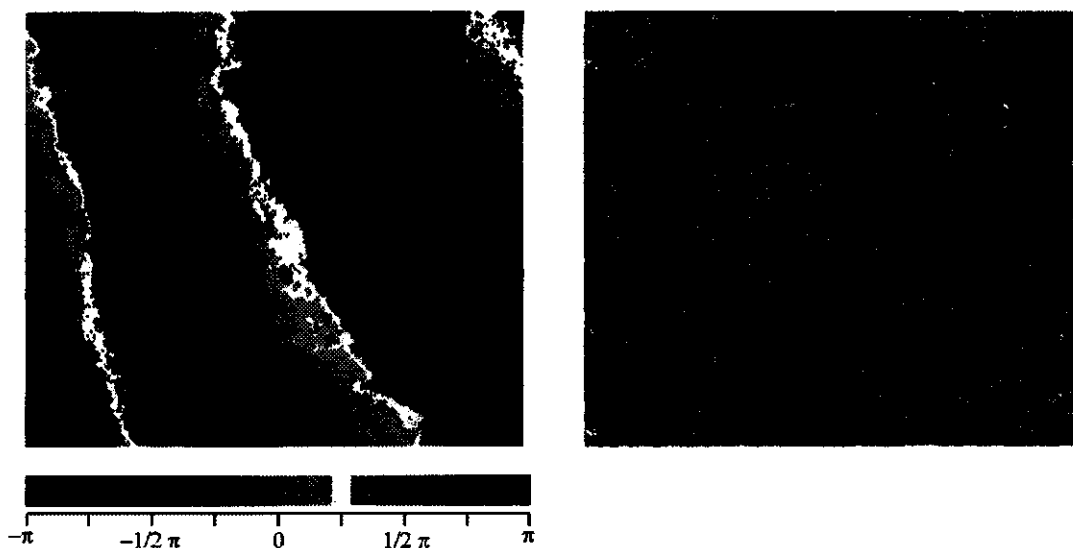
Figure 5.10: Phase images of the Barrax test area

it is impossible to distinguish a baseline angle knowledge error from a slope on the surface topography (see Figure 5.9). Thus a change in incidence angle $d\theta_{inc}$ is the same as a change in baseline angle $d\alpha$. The most important effect of this attitude error is the introduction of a tilt across the radar swath, resulting in a common error for a large area. These error can be corrected or diminished by using knowledge of the height of a few point s in a given scene. The phase error will increase the statistical variation of each point in the DEM.

First results over test sites in the Netherlands by FEL-TNO, using data separated 3 days in time, show its usefulness in deriving information on vegetation which is related to biomass, height and rate of growth. Also small changes (in the millimeter range) in height of the surface are sometimes measured. Under certain conditions these could be interpreted as the swelling/shrinking of clays. Under other conditions however, it may be related to soil moisture variation (the dry crust is more or less transparent to microwaves). The technique seems to be affected by adverse atmospheric conditions (heavy cloud cover and rain reduce propagation speed) but seems to work very good under dry conditions such as usually encountered in the Mediterranean.

For the Barrax/Castilla-La Mancha area coherency and phase maps (interferograms) are produced for two sets of observations. Namely the pair of ERS-1 of May 24 and May 25 and the pair of June 4 and August 13, 1996. Theoretically the coherence between two images reduces to zero for the ERS satellites at a perpendicular baseline of approximately 1100m. However, at 836 m this coherence is already too small to produce an interferogram with acceptable coherence for our research aims ((Halsema, 1998)). The two pairs above were the only pairs with an acceptable baseline.In Figure 5.10 and Figure 5.11 the phase maps and coherency maps of the two pairs are given. In Figure 5.12 the intensity images are given for reference. The difference in the two pairs is obvious in the first pair (May 24 and 25) there is a high coherence and therefore the phase images shows very clear fringes. In the second pair (June 4 and August 13) the coherence is much lower and therefore the fringes are not clear in the phase images. The latter is probably due to the differences in variation of the vegetation. High coherence will be present for those objects that do not change much (either in shape or dielectric properties) and do have a change
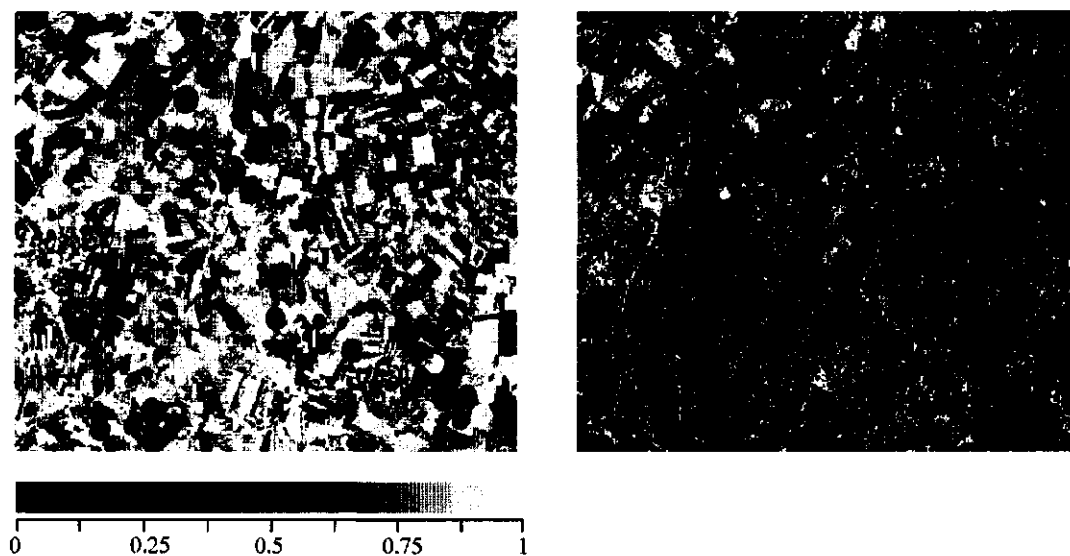
Figure 5.11: Coherence images of the Barrax test area.
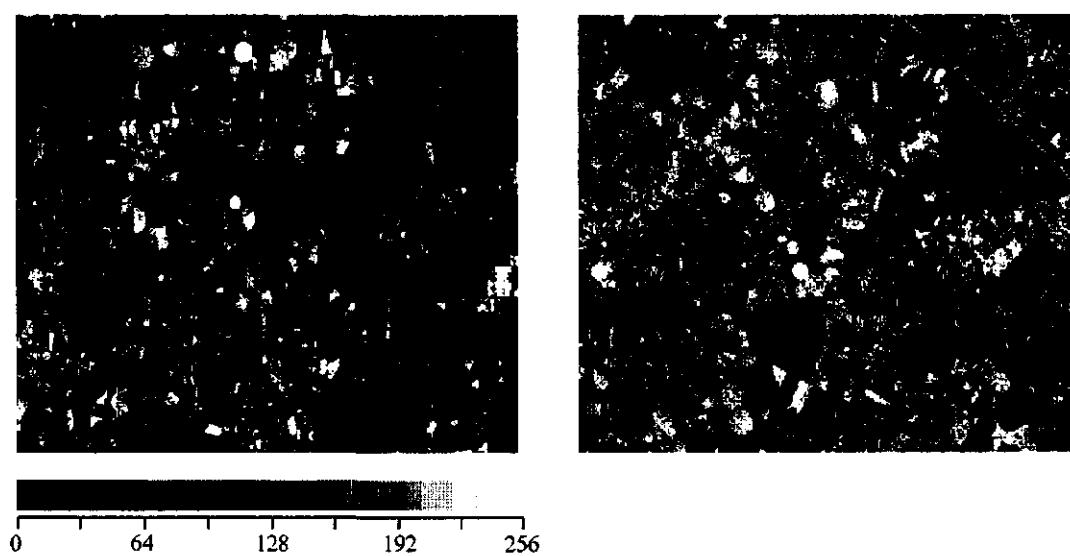
Figure 5.12: Intensity images (scaled, DN) of the Barrax test area
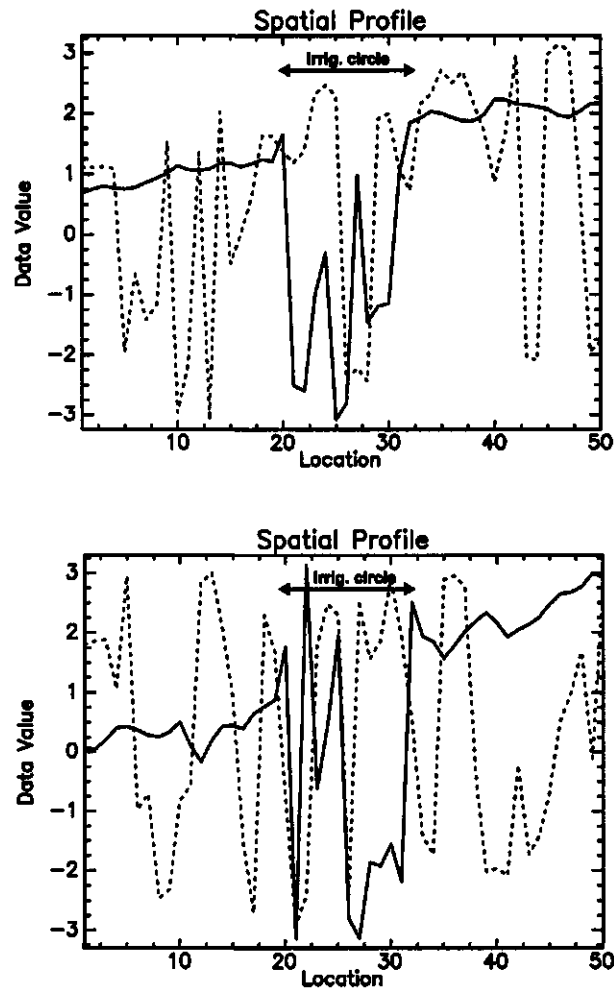
Figure 5.13: Two profiles of transects over a (partly wet) irrigation circle in the interferogram. Notice that the phases are significantly different over the irrigated area.

in height which might give rise to a change in phase. For the first pair with only 24 hours in between the coherence is very high and only changes due to irrigation can be clearly noted (See the circular shapes in the left of Figure 5.10).

In Figure 5.13 the phase changes over two transects across a pivot irrigation circle are given. The drop in phase indicates the difference with the surrounding dry area. The average phase change is about . It still has to be investigated how this information can be converted to represent correct soil moisture changes.

The use of interferometry for change detection in geo- and biophysical parameters is only very useful when data pairs are available that have naturally a short baseline but also are close to each other in time. For longer time periods most biophysical parameters are so variable that coherence is greatly diminished. To extract information on variables such as soil moisture is only feasible when other factors remain constant. Further research will done on these data to more precisely determine the conditions under which soil moisture determination is feasible and what type of changes of vegetation can be characterized.

# Acknowledgements

# References

Attema, E. & Ulaby, F. (1978). Vegetation modelled as a water cloud. *Radio Science*, 13, 357–364.

Bolle, H., Ed. (1995). *Remote sensing of Mediterranean desertification and environmental changes RESMEDES*. Research Proposal in response to the Framework IV, 1994-1998, of the European Commission on Environment and climate.

Bolle, H. & Streckenbach, B. (1992). *The ECHIVAL Field Experiment in a Desertification threatened Area*. Technical report, EFEDA-Secretariat, Free University of Berlin. First Annual Report to EC.

Chauhan, N. (1995). Microwave inversion of root mean square height from vegetated fields: a dual frequency technique. *Int. J. Remote Sensing*, 16(18), 3555–3567.

Chen, K., Yen, S., & Huang, W. (1995). A simple model for retrieving bare soil moisture from radar-scattering coefficients. *Remote Sens. Environ.*, 54, 121–126.

Dasberg, S. & Dalton, F. (1985). Time domain reflectometry field measurements os soil water content and electrical conductivity. *Soil Sci. Soc. Am. J.*, 49, 293–297.

Dubois, P., van Zyl, J., & Engman, E. (1995). Measuring soil moisture with imaging radars. *IEEE Trans. Geosci. Remote Sensing*, 33(4), 915–26. Corrections in: 33(6):1340, November, 1995.

Engman, E. & Chauhan, N. (1995). Status of microwave soil moisture measurements with remote sensing. *Remote Sens. Environ.*, 51, 189–198.

Fung, A. (1994). *Microwave scattering and emission models and their applications*. Artech House, Norwood.

Fung, A., Dawson, M., Chen, K., Hsu, A., Engman, E., O'Neill, P., & Wang, J. (1996). A modified iem model for scattering from surfaces with application to soil moisture sensing. In *Proceedings IGARSS'96* (pp. 1297–1299).: IEEE.

Fung, A., Li, Z., & Chen, K. (1992). Backscattering from a randomly rough dielectric surface. *IEEE Trans. Geosci. Remote Sensing*, 30(2), 356–369.

Halsema, E. (1998). Personal Communication.

Heimovaara, T. & Bouten, W. (1990). A computer controlled 36-channel time domain reflectometry system for monitoring soil water contents. *Water Resources Research*, 26(10), 2311–2316.

Houghton, J. (1977). *The Physics of Atmospheres*. Cambridge: Cambridge University Press.

Ji, J., Keur, P. v., Thomson, A., & Skriver, H. (1996). Soil moisture retrieval using the danish l- c-band polarimetric SAR. In *Proceedings IGARSS'96* (pp. 1300–1302).

Karam, M., Fung, A., Lang, R., & Chauhan, N. (1992). A microwave scattering model for layered vegetation. *IEEE Trans. Geosci. Remote Sensing*, 30(4), 767–784.

Ogilvy, J. (1990). *Theory of wave scattering from random rough surfaces.* Redcliffe Way, Bristol, BS1 6NX: IOP Publishing Ltd.

Press, W., Teukolsky, S., Vetterlin, W., & Flannery, B. (1992). *Numerical Recipes in FORTRAN. The art of scientific computing.* Cambridge University Press, 2nd edition.

Rodgers, C. D. (1976). Retrieval of atmospheric temperature and composition from remote measurements of thermal radiation. *Reviews of Geophysics and Space Physics*, 14(4), 609–624.

Ulaby, F., Moore, R., & Fung, A. (1986). *Microwave Remote Sensing: active and passive*, volume III From theory to applications. Artech House, Norwood.

van Oevelen, P. & Hoekman, D. (1994). Estimation of areal soil water content during HAPEX-Sahel and EFEDA-Spain. *Proc. IGARSS'94*, (pp. 1591–1592).

van Oevelen, P. & Hoekman, D. (1998). Radar backscatter inversion techniques for estimation of surface soil moisture: EFEDA-Spain and HAPEX-Sahel case studies. *IEEE Trans. Geosci. Remote Sensing.* Accepted for publication.

Vissers, M. & Hoekman, D. (1991). Efeda-spain: a ground truth data collection report.

Wismann, V., Cavanie, A., Hoekman, D., Woodhouse, I., Boehnke, K., & Schmullius, C. (1996). *Land surface observations using the ERS-1 windscatterometer.* Final report for European Space Agency (contract no. 11103/94/NL/CN), Institute for Applied Remote Sensing, Wedel, Germany.

Zebker, H. A., Wernber, C. L., Rosen, P. A., & Hensley, S. (1994). Accuracy of topographic maps derived from ers-1 interferomteric radar. *IEEE Trans. Geosci. and Remote Sensing*, 32(4), 823–836.

# Appendix A

# Soil moisture measurements

Table A.1: TDR soil moisture measurements along transects 1 and 2 as indicated in Figure 3.2.

| Sample # | $\theta$ (Martin) [%] | Description Lat/long | $\theta$ (Peter)[1] [%] | Description Lat/long |
|---|---|---|---|---|
| 1 | 3.5 | | 3.6 | $39°03'16N$ $2°04'95''W$ |
| 2 | 5.4 | | 4.7 | |
| 3 | 4.6 | | 4.8 | |
| 4 | 5.6 | | 7.2 | |
| 5 | 4.9 | | 8.5 | |
| 6 | 4.5 | | 6.7 | |
| 7 | 5.1 | | 6.8 | |
| 8 | 4 | | 7.7 | |
| 9 | 5.3 | | 9.6 | |
| 10 | 4.8 | | 5.9 | |
| 11 | 4.8 | | 4.8 | |
| 12 | 4.8 | | 5.8 | |
| 13 | 2.9 | | 8 | |
| 14 | 5.6 | | 5.9 | |
| 15 | 3.3 | | 7.4 | |
| 16 | 4.8 | $39°03'24''N$ $2°05'07''W$ | 5.9 | |
| 17 | - | | 8.6 | |
| 18 | 4.2 | | 6.2 | |
| 19 | - | | 6.9 | |
| 20 | 2.8 | | 9.1 | |
| 21 | - | | 7.6 | |
| 22 | 5.6 | | 5.3 | |
| 23 | - | | 7.1 | |
| 24 | 2.6 | | 10.3 | |
| 25 | - | | 7 | |
| 26 | 5.8 | | 6.3 | |
| 27 | 4.8 | $39°03'25''N$ $2°05'12''W$ | 10.8 | |

Continued on the next page.

| Sample # | θ (Martin) [%] | Description Lat/long | θ (Peter)[2] [%] | Description Lat/long |
|---|---|---|---|---|
| 1 | 3.5 | | 3.6 | 39°03′16N 2°04′95″W |
| 28 | 5.4 | | 4.9 | |
| 29 | 6.8 | | 6.4 | |
| 30 | 4.3 | | 8.8 | |
| 31 | 5 | | 10.7 | |
| 32 | 4.1 | 39°03′30″N 2°05′15″W | 10.9 | |
| 33 | 4.8 | | 3 | |
| 34 | 7.3 | | 6.3 | |
| 35 | 6.5 | | 12.3 | |
| 36 | 5.9 | | 10.7 | |
| 37 | 6 | | 9.2 | |
| 38 | 5 | | 5.6 | |
| 39 | 2.3 | | 6.4 | |
| 40 | 5.2 | | 7.4 | |
| 41 | 3.2 | | 9.7 | |
| 42 | 6.1 | 39°03′31″N 2°05′17″W | 9.8 | |
| 43 | 3.2 | | 8.8 | |
| 44 | 3.1 | | 6.8 | |
| 45 | 4.9 | | 7.3 | |
| 46 | 5.2 | | 4.1 | |
| 47 | 3.1 | | 16.6 | |
| 48 | 9 | Wheeltracks | 7.9 | |
| 49 | 10.9 | Wheeltracks | 11.8 | |
| 50 | 5.1 | | 14.1 | |
| 51 | 6.9 | 39°03′35″N 2°05′29″W | 3.4 | |
| 52 | 4.5 | | 5.9 | |
| 53 | 7.2 | | 11.9 | |
| 54 | 8.1 | | 7.4 | |
| 55 | 6.6 | | 7.2 | |
| 56 | 3.4 | | 7.6 | |
| 57 | 4.9 | | 5.2 | |
| 58 | 5.2 | | 7.8 | |
| 59 | 5.1 | | 7 | |
| 60 | 3.5 | | 7.5 | |
| 61 | 4.9 | 39°03′38″N 2°05′37″W | 6.6 | |
| 62 | 3 | | 5.9 | |
| 63 | 4.4 | | 9.5 | |
| 64 | 5.5 | | 7.1 | |
| 65 | 3 | | 7.2 | |
| 66 | 4.5 | | 14.2 | |
| 67 | 4.8 | | - | |
| 68 | 5.4 | | - | |
| 69 | 5.6 | | - | |
| 70 | 4.4 | | 18.7 | Start beets |

| Sample # | $\theta$ (Martin) [%] | Description Lat/long | $\theta$ (Peter)[2] [%] | Description Lat/long |
|---|---|---|---|---|
| 1 | 3.5 | | 3.6 | 39°03'16N 2°04'95"W |
| 71 | 5.2 | 39°03'41"N 2°05'44"W | 15.3 | |
| 72 | 12 | | 19.4 | |
| 73 | 4 | Edge of bare | 15.2 | |
| 74 | - | Fallow | 14.6 | |
| 75 | 12.7 | Start beets | 19.5 | |
| 76 | 6.8 | | 16.7 | |
| 77 | 12.3 | | 14.5 | |
| 78 | 11.5 | | 13.5 | |
| 79 | 14.1 | | 23.9 | |
| 80 | 18.4 | | 13.6 | |
| 81 | 10.5 | 39°03'42N 2°05'49"W | 13.9 | |
| 82 | 10.8 | | 15.1 | |
| 83 | 12.9 | | 14.6 | |
| 84 | 11.8 | | 14.6 | |
| 85 | 9.8 | | 14 | |
| 86 | 9.8 | | 13.9 | |
| 87 | 12.2 | | 17.5 | |
| 88 | 14.9 | | 19.7 | |
| 89 | 11 | 39°03'43N 2°05'57"W | 20 | |
| 90 | 11.4 | | 16.1 | |
| 91 | 11 | | 27.5 | |
| 92 | 14.5 | | 17 | |
| 93 | 16 | | 15.3 | |
| 94 | 12.6 | | 18.1 | |
| 95 | 13.7 | | 24.5 | |
| 96 | 16.8 | | 18.8 | |
| 97 | 13.1 | | 19 | |
| 98 | 11.7 | | 12.4 | |
| 99 | 14.3 | | 11.3 | |
| 100 | 12.3 | | 22.5 | |
| 101 | 13.1 | 39°03'49"N 2°05'64"W | 15.6 | |
| 102 | 14.1 | | 14.3 | |
| 103 | 11.5 | | 11.7 | |
| 104 | 18.2 | | 14.4 | |
| 105 | 12.6 | | - | |
| 106 | 13.4 | | - | centre pivot |
| 107 | 10.4 | | 10.3 | |
| 108 | 10.6 | | 13.7 | |
| 109 | 13.6 | | 14.3 | |
| 110 | 13.4 | | 16.2 | |
| 111 | 12.9 | 39°03'52"N 2°05'71"W | 24.2 | |
| 112 | 16.3 | | 19.8 | |

Continued on the next page.

| Sample # | $\theta$ (Martin) [%] | Description Lat/long | $\theta$ (Peter)[2] [%] | Description Lat/long |
|---|---|---|---|---|
| 1 | 3.5 | | 3.6 | 39°03'16N 2°04'95"W |
| 113 | 10.4 | At pivot boom | 15.7 | |
| 114 | 11.9 | | 15.7 | |
| 115 | 21.6 | | 14.6 | |
| 116 | 16.3 | | 17.4 | |
| 117 | 13.5 | | 17.6 | |
| 118 | 12.4 | | 16.8 | |
| 119 | 7.9 | | 16 | |
| 120 | 14.4 | | 22 | |
| 121 | 11.4 | 39°03'53"N 2°05'79"W | 20 | |
| 122 | 9.4 | | 14.2 | |
| 123 | 12.1 | | 15.9 | |
| 124 | 7.8 | | 18.3 | |
| 125 | 14.7 | | 12.6 | |
| 126 | 17.4 | | 13.8 | |
| 127 | 14.6 | | 15.3 | |
| 128 | 20.9 | | 13.1 | |
| 129 | 10.1 | | 10.8 | |
| 130 | 14.1 | | 16.9 | |
| 131 | 11.5 | 39°03'56"N 2°05'86"W | 19.1 | |
| 132 | 16.2 | | 16 | |
| 133 | 6.1 | | 20.2 | |
| 134 | 12.7 | | 15.8 | |
| 135 | 9.3 | | 12.9 | |
| 136 | 6.7 | | 15.9 | |
| 137 | 11.5 | | 14.6 | |
| 138 | 10.9 | | 15.5 | |
| 139 | 14.6 | | 16.3 | |
| 140 | 15.5 | | 16.5 | |
| 141 | 11.6 | 39°03'57"N 2°05'93"W | 16.4 | |
| 142 | 9.9 | | 6.6 | End beets |
| 143 | 16.4 | | | 39°03'58"N 2°05'93"W |
| 144 | 11.2 | | | |
| 145 | 12.9 | End beets | | |

End of Table

---

Table A.2: TDR soil moisture measurements on along transects 1 and 2 as indicated in Figure 3.2.

| Sample # 25/5/96 *start*8.00*h* | $\theta$ (Martin) [%] | Description Lat/long 26 steps | $\theta$ (Peter)[3] [%] | Description Lat/long 25 m |
|---|---|---|---|---|
| 1 | 4.6 | | 3.3 | 39°03′16″ 2°04′96″ |
| 2 | 4.5 | | 4.3 | |
| 3 | 4.2 | | 6.4 | |
| 4 | 2.6 | | 9 | |
| 5 | 4.6 | | 3.8 | |
| 6 | 3.5 | | 4.7 | |
| 7 | 4.8 | | 7.6 | |
| 8 | 3.8 | | 2.2 | |
| 9 | 4.6 | | 0.06 | |
| 10 | 4.3 | | 4.7 | 39°03′4″ 2°05′09″ |
| 11 | 3 | | 6.6 | |
| 12 | 5.2 | | 5.5 | |
| 13 | 3.3 | | 3 | different roughness |
| 14 | 5.1 | 2nd roughness | 5.2 | |
| 15 | 6.2 | | 6.9 | |
| 16 | 5.2 | | 6.2 | |
| 17 | 4.3 | | 5.3 | |
| 18 | 7.1 | | 5.4 | |
| 19 | 5.8 | | 6.7 | |
| 20 | 5.5 | | 2.7 | 39°03′23″ 2°05′19″ |
| 21 | 2.6 | tractor circles | 4.3 | |
| 22 | 3.8 | 3rd roughness | 4.4 | |
| 23 | 5.1 | | 3.1 | |
| 24 | 2.4 | | 3.2 | |
| 25 | 2.1 | | 4.3 | |
| 26 | 4.7 | | 8.1 | |
| 27 | 4.9 | | 9.2 | |
| 28 | 4.3 | | 3.3 | |
| 29 | 4.2 | | 5.7 | |
| 30 | 4.5 | | 5.1 | 39°03′28″ 2°05′37″ |
| 31 | 3.5 | | 6.3 | |
| 32 | 3.9 | | 3.5 | |
| 33 | 8.8 | tractor tracks | 2.7 | |
| 34 | 5.2 | | 6 | |
| 35 | 3.4 | | 4.3 | |
| 36 | 5 | | 7.3 | |
| 37 | 6.6 | | 8.6 | end bare |
| 38 | 3.8 | 21 steps to end bare fld | | |
| 39 | 5.2 | 21 steps to begin beets | 13.7 | begin beets |

Continued on the next page.

| Sample # 25/5/96 start8.00h | $\theta$ (Martin) [%] | Description Lat/long 26 steps | $\theta$ (Peter)[4] [%] | Description Lat/long 25 m |
|---|---|---|---|---|
| 40 | 15.7 | | 14.8 | 39°03′39″ 2°05′42″ |
| 41 | 8.4 | | 16.6 | |
| 42 | 11.5 | | 23.3 | |
| 43 | 9 | | 11.8 | |
| 44 | 9 | | 16.5 | |
| 45 | 10.4 | | 12.5 | |
| 46 | 14.3 | | 4.5 | |
| 47 | 7 | | 16.7 | |
| 48 | 7.3 | | 12.8 | |
| 49 | 10.1 | | 16.4 | |
| 50 | 13.7 | | 16.3 | |
| 51 | 8.4 | | 21.6 | |
| 52 | 14 | | 10.1 | 39°03′45″ 2°05′65″ |
| 53 | 15.1 | | 16.1 | |
| 54 | 12.9 | | 15 | |
| 55 | 15.4 | harrowed part | 12.9 | |
| 56 | 14.9 | | | centre pivot turns count. cw. |
| 57 | 18 | | 29.2 | start irrigated part |
| 58 | 7 | | 18.6 | |
| 59 | 8.3 | | 27.4 | |
| 60 | 12.6 | | 25.2 | 39°03′47″ 2°05′81″ |
| 61 | 23.3 | start irrigated part | 25.4 | |
| 62 | 19.2 | | 21.2 | |
| 63 | 21.9 | | 26.4 | |
| 64 | 29.4 | | 31.3 | |
| 65 | 22.1 | | 26.1 | |
| 66 | 19.7 | | 27 | |
| 67 | 22.5 | | 25.5 | |
| 68 | 18.2 | | 22.9 | |
| 69 | 20.4 | | 18 | |
| 70 | 17.9 | | 21.3 | 39°03′43″ 2°05′97″ |
| 71 | 18.4 | | 19.4 | |
| 72 | 22.3 | | 17.3 | |
| 73 | 15.8 | | 26.4 | 39°03′45″ 2°06′05″ |
| 74 | 16.2 | | | |
| 75 | 18.9 | | | |

End of Table

---

[4] Instument Trime TDR ser. no. 1437

Table A.3: TDR soil moisture measurements performed on a former leek field, field 3 in Figure 3.2.

| Sample # | $\theta$ (Martin) [%] | Description Lat/long | $\theta$ (Peter)[5] [%] | Description Lat/long |
|---|---|---|---|---|
| 1 | 18.2 | 39°04'07"N 2°05'89"W | | |
| | 21.1 | 39°04'07" 2°05'85" | | |
| 2 | 10.3 | | 12.8 | |
| 3 | 6.9 | | 15.1 | |
| 4 | 4.2 | | 12.6 | |
| 5 | 4.4 | | 12.1 | 39°04'08" 2°05'86" |
| 6 | 4.6 | | 9.9 | |
| 7 | 6.2 | | 11.7 | |
| 8 | 6.3 | | 10 | |
| 9 | 5.8 | | 11.8 | |
| 10 | 9.4 | | 11.3 | 39°04'08" 2°05'89" |
| 11 | 5.9 | | 9.6 | |
| 12 | 5.7 | | 15 | |
| 13 | 6.6 | | 11.4 | |
| 14 | 6.9 | | 11.3 | |
| 15 | 7.7 | | 7.6 | 39°04'24" 2°05'86" |
| 16 | 5.4 | | 11.4 | |
| 17 | 8.4 | | 13.9 | |
| 18 | 9.4 | | 6.5 | |
| 19 | 4.6 | | 11.9 | |
| 20 | 7.5 | | 8.4 | 39°04'16" 2°05'92" |
| 21 | 8.9 | | 12.2 | |
| 22 | 4.5 | | 14.5 | |
| 23 | 7.1 | | 10.9 | |
| 24 | 6.4 | | 8.9 | |
| 25 | 5.7 | | 10.8 | 39°04'17" 2°05'93" |
| 26 | 5.6 | | 7.3 | |
| 27 | 9 | | 8.5 | |
| 28 | 5.8 | | 8.7 | |
| 29 | 6.8 | | 10.9 | |
| 30 | 5.9 | | 9.1 | 39°04'06" 2°05'99" |
| 31 | 4.8 | | 9.1 | |
| 32 | 6.3 | | 4.7 | |
| 33 | 5.7 | | 15.5 | |
| 34 | 9.2 | | 9 | |
| 35 | 12.9 | end part quarter field | 7.6 | 39°04'14" 2°06'00" |

| Sample # | $\theta$ (Martin) [%] | Description Lat/long | $\theta$ (Peter)[6] [%] | Description Lat/long |
|---|---|---|---|---|
| 1 | 18.2 | 39°04'07"$N$ 2°05'89"$W$ | | |
| 36 | - | 2nd to last wheel track | 8.5 | |
| 37 | - | 39°04'13" 2°06'07" | 8.3 | |
| 38 | - | | 9.2 | |
| 39 | - | | 9.5 | |
| 40 | - | | 15.5 | 39°04'15" 2°06'03" |
| 41 | - | | 10.8 | |
| 42 | - | | 14.9 | |
| 43 | - | | 14.6 | |
| 44 | - | | 15.3 | |
| 45 | - | | 11.7 | 39°04'21" 2°06'05" |

End of Table

---

[6] Instument Trime TDR ser. no. 1437

# Appendix B

# Surface roughness measurements

| # | Direction | Slope [-] | $\sigma_{uncor}$ [mm] | $\sigma_{cor}$ [mm] | $l_{exp.}$ [cm] | $l_{Gaussian}$ [cm] |
|---|---|---|---|---|---|---|
| 1a | ppd1 | 0.0636364 | 10.0782 | 8.90880 | 8.92120 | 11.0617 |
| 1b | ppd2 | 0.0394139 | 20.1231 | 19.9103 | 26.9196 | 31.2527 |
| 1c | par1 | 0.309197 | 26.1612 | 12.6590 | 11.9128 | 14.5349 |
| 1d | par2 | -0.153794 | 21.1518 | 17.8247 | 8.00030 | 10.1433 |
| 2a | ppd1 | 0.416660 | 35.6812 | 17.9256 | 18.1457 | 21.9915 |
| 2b | ppd2 | 0.0559678 | 25.5526 | 25.2143 | 21.3000 | 24.6426 |
| 2c | par1 | 0.0257231 | 8.71248 | 8.50174 | 9.96417 | 12.1040 |
| 2d | par2 | 0.128037 | 12.5871 | 8.27981 | 4.82657 | 5.79282 |
| 2e | - | -0.00264392 | 46.2985 | 46.2980 | 13.0912 | 14.8589 |
| 2f | ppd1 | 0.00828611 | 14.6074 | 14.5945 | 11.5857 | 13.6516 |
| 2g | ppd2 | -0.129994 | 27.5347 | 25.7975 | 15.7264 | 18.2280 |
| 2h | par1 | 0.0804225 | 8.25957 | 5.72360 | 7.57104 | 7.28641 |
| 2i | par2 | -0.0408919 | 5.88268 | 5.04363 | 14.9987 | 18.3817 |
| 3a | ppd1 | -0.188553 | 24.0300 | 19.5582 | 4.35911 | 5.47136 |
| 3b | ppd2 | -0.0897856 | 24.7073 | 23.7960 | 6.01658 | 7.54956 |
| 3c | par1 | -0.0301587 | 18.5020 | 18.3668 | 3.47222 | 3.98577 |
| 3d | par2 | -0.0372337 | 25.2900 | 25.1393 | 3.97114 | 4.97019 |
| 4a | ppd1 | 0.0545631 | 27.7045 | 27.4084 | 9.57194 | 11.7756 |
| 4b | ppd2 | 0.0934631 | 30.6761 | 29.8852 | 14.3624 | 17.1880 |
| 4c | par1 | -0.271477 | 26.5639 | 17.3657 | 7.19019 | 9.03727 |
| 4d | par2 | -0.148895 | 31.3047 | 29.2991 | 15.7771 | 17.8632 |
| 5a | ppd1 | -0.0771646 | 27.4751 | 26.8744 | 10.7062 | 13.0614 |
| 5b | ppd2 | 0.207046 | 23.4663 | 17.7661 | 8.11598 | 9.95820 |
| 5c | par1 | 0.135246 | 19.8305 | 17.1161 | 3.58446 | 4.25272 |
| 5d | par2 | 0.127983 | 19.3469 | 16.8671 | 3.59769 | 4.41366 |
| 6a | ppd1 | 0.433013 | 52.1201 | 41.0914 | 22.3162 | 26.6892 |
| 6b | ppd2 | 0.120598 | 32.8631 | 31.6267 | 12.6336 | 14.9505 |
| 6c | par1 | 0.0593824 | 21.7546 | 21.3056 | 4.27648 | 5.33462 |
| 6d | par2 | 0.121722 | 25.4961 | 23.8499 | 9.12348 | 5.79066 |
| 7a | ppd1 | 0.0362207 | 15.5396 | 15.3064 | 25.6632 | 30.1912 |
| 7b | ppd2 | -0.0192359 | 10.1401 | 10.0396 | 1.75207 | - |
| 7c | par1 | 0.113415 | 15.5020 | 13.0303 | 4.93798 | 5.86478 |
| 7d | par2 | 0.158847 | 19.8701 | 16.0150 | 35.6859 | 39.7326 |

Table B.1: Surface roughness data measurements taken on the 25 May, 1996 at the ITAP experimental farm. The numbers indicate the plots.
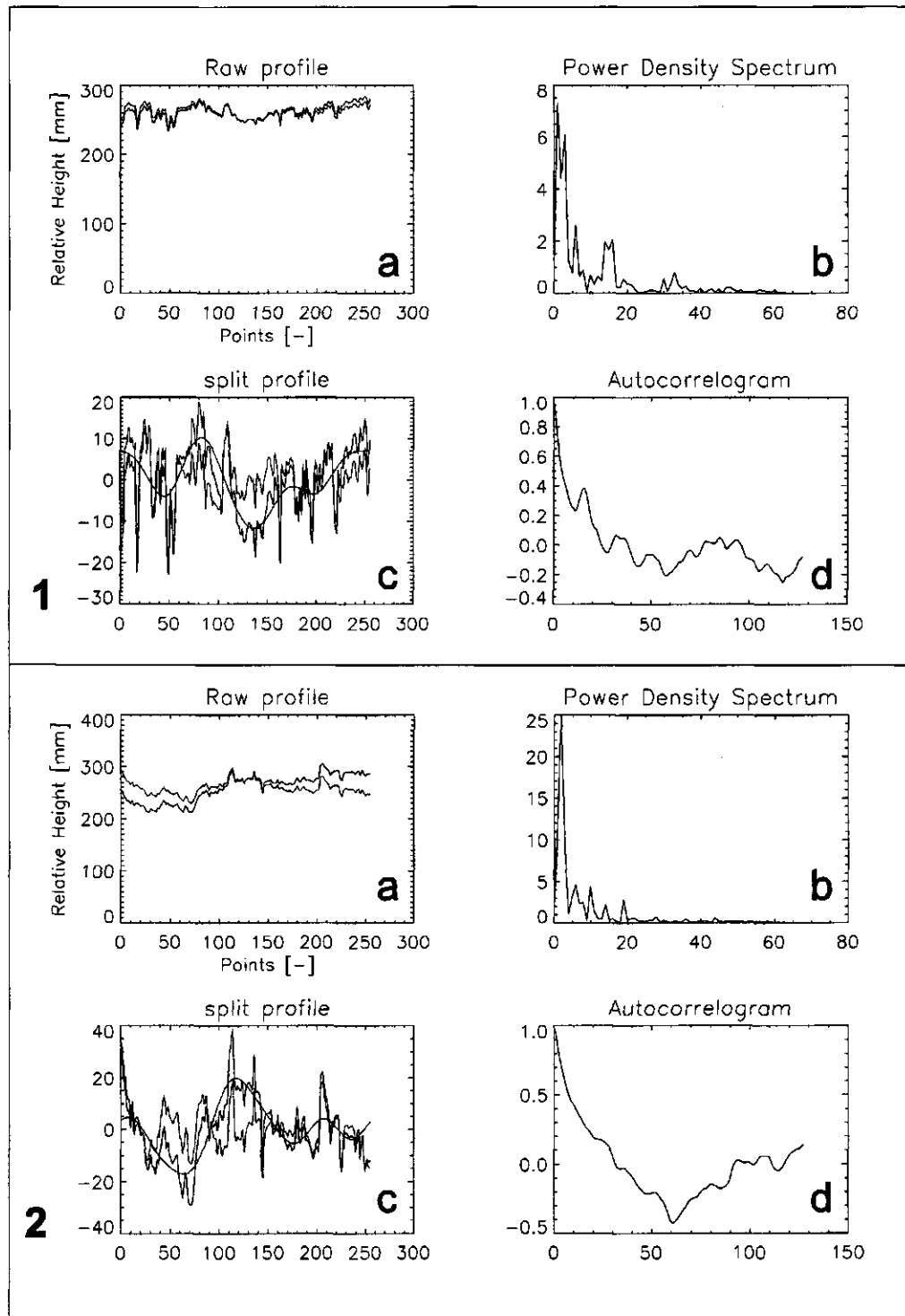
Figure B.1: Raw profile, Power density spectrum, Split profile and Autocorrelogram of the surface roughness data measurements of 1a and 1b
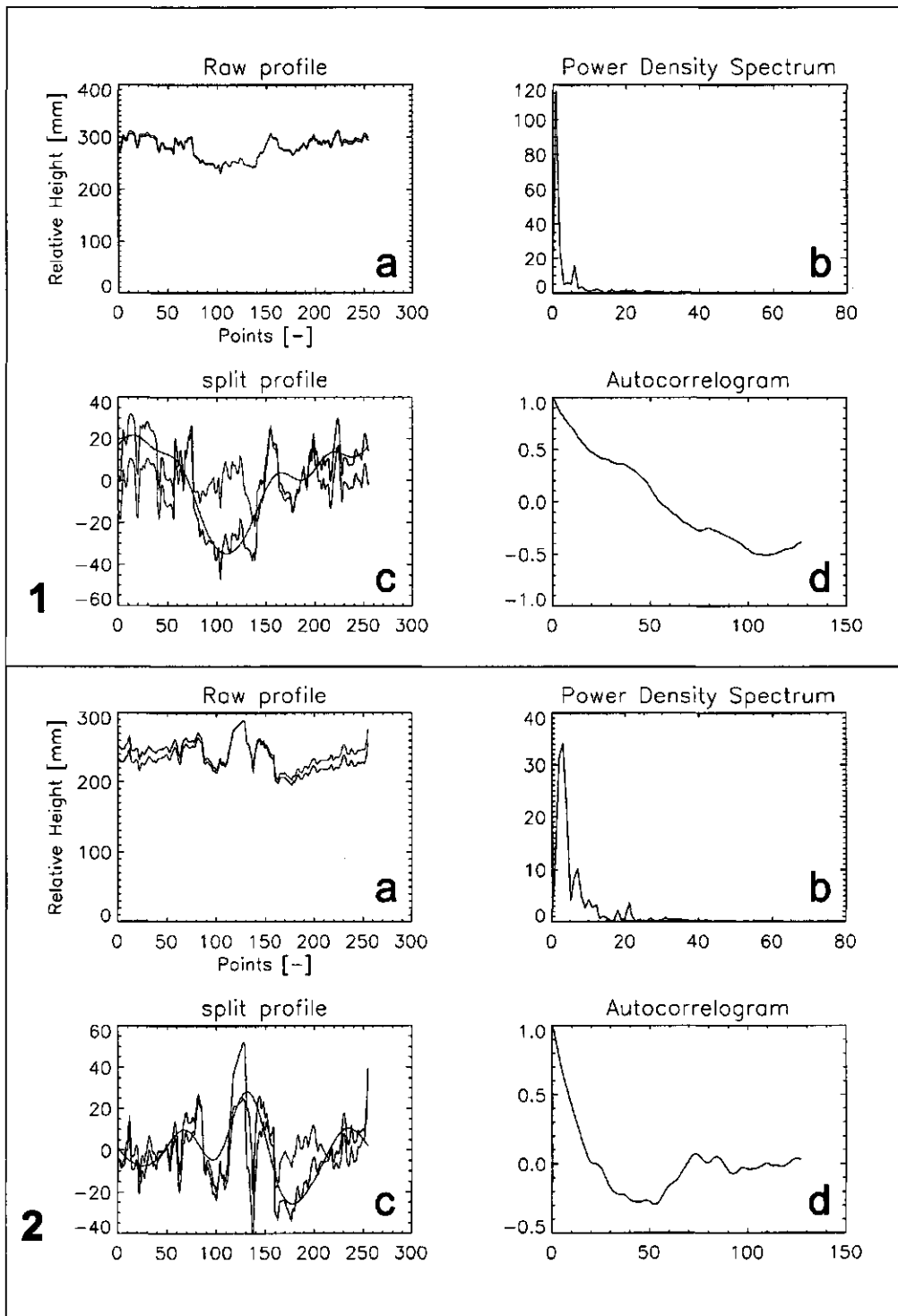
Figure B.2: Raw profile, Power density spectrum, Split profile and Autocorrelogram of the surface roughness data measurements of 1c and 1d
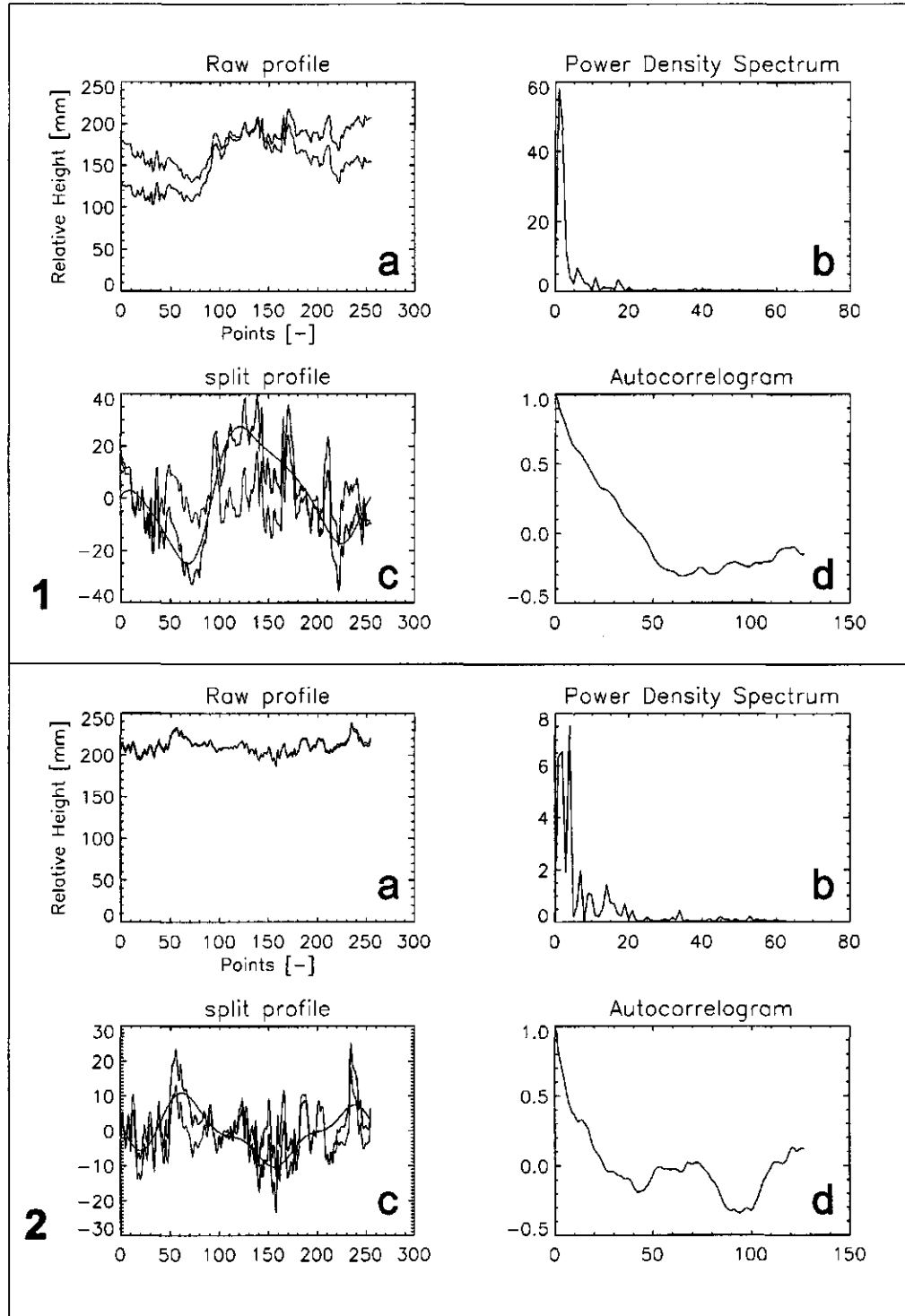
Figure B.3: Raw profile, Power density spectrum, Split profile and Autocorrelogram
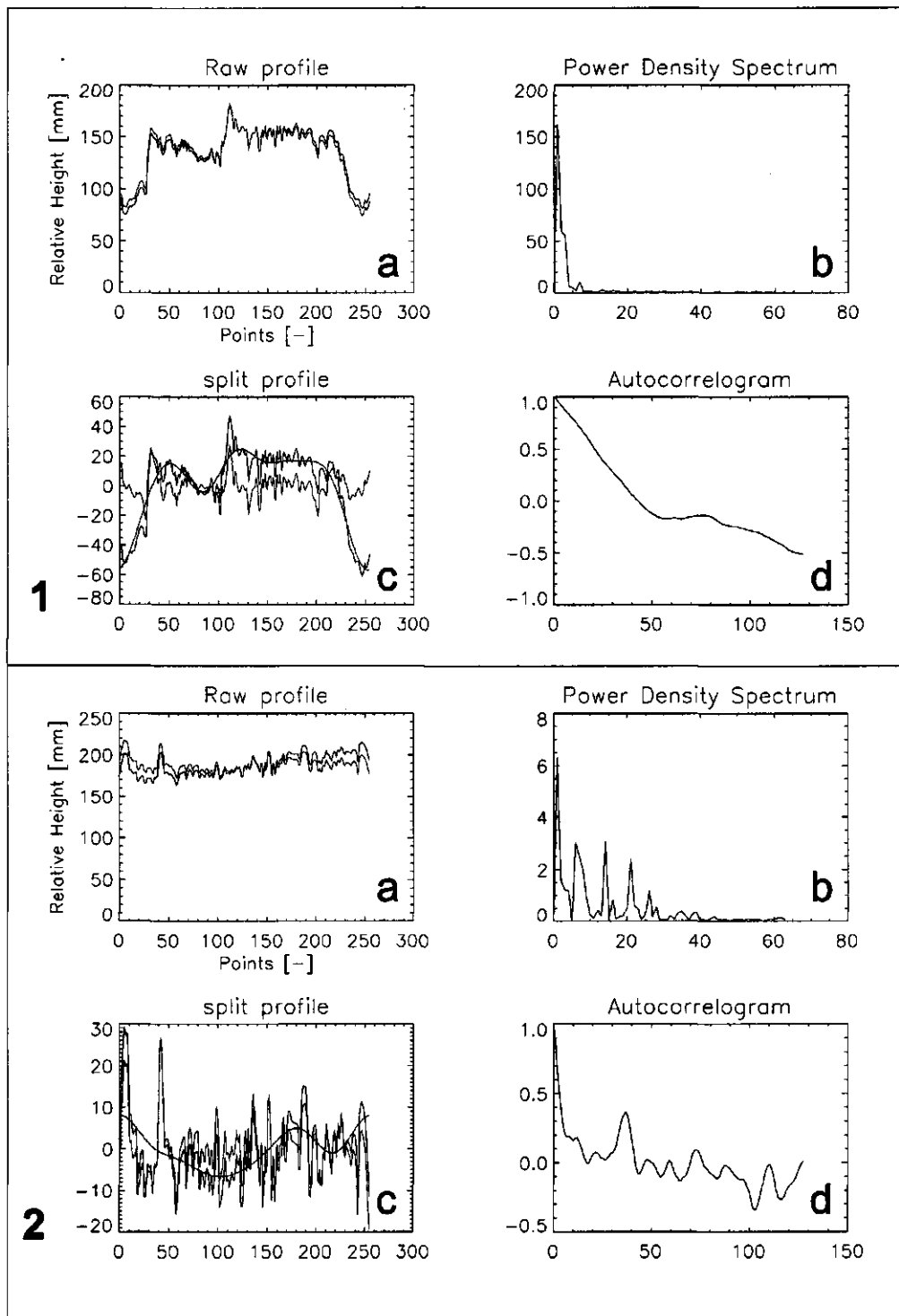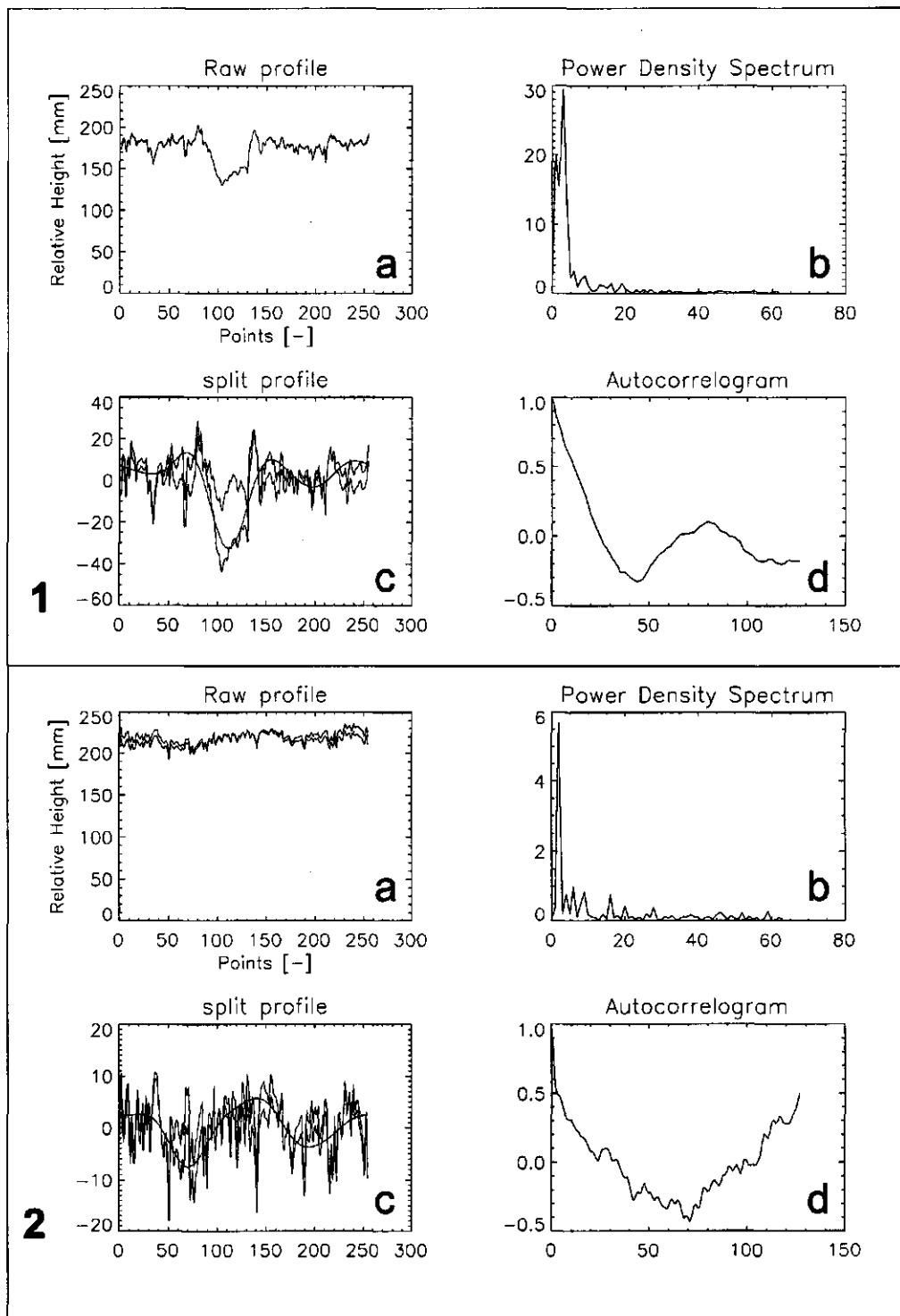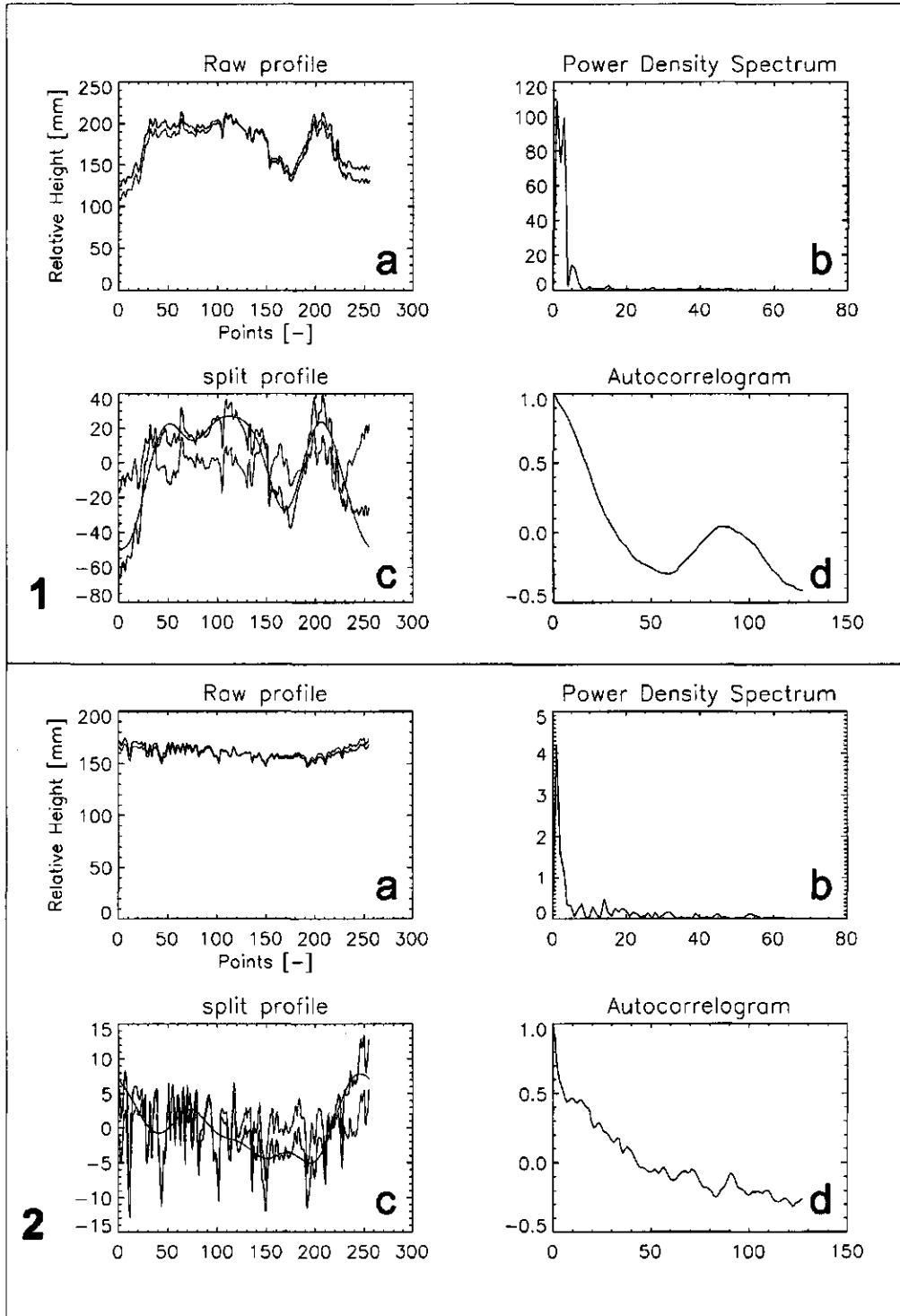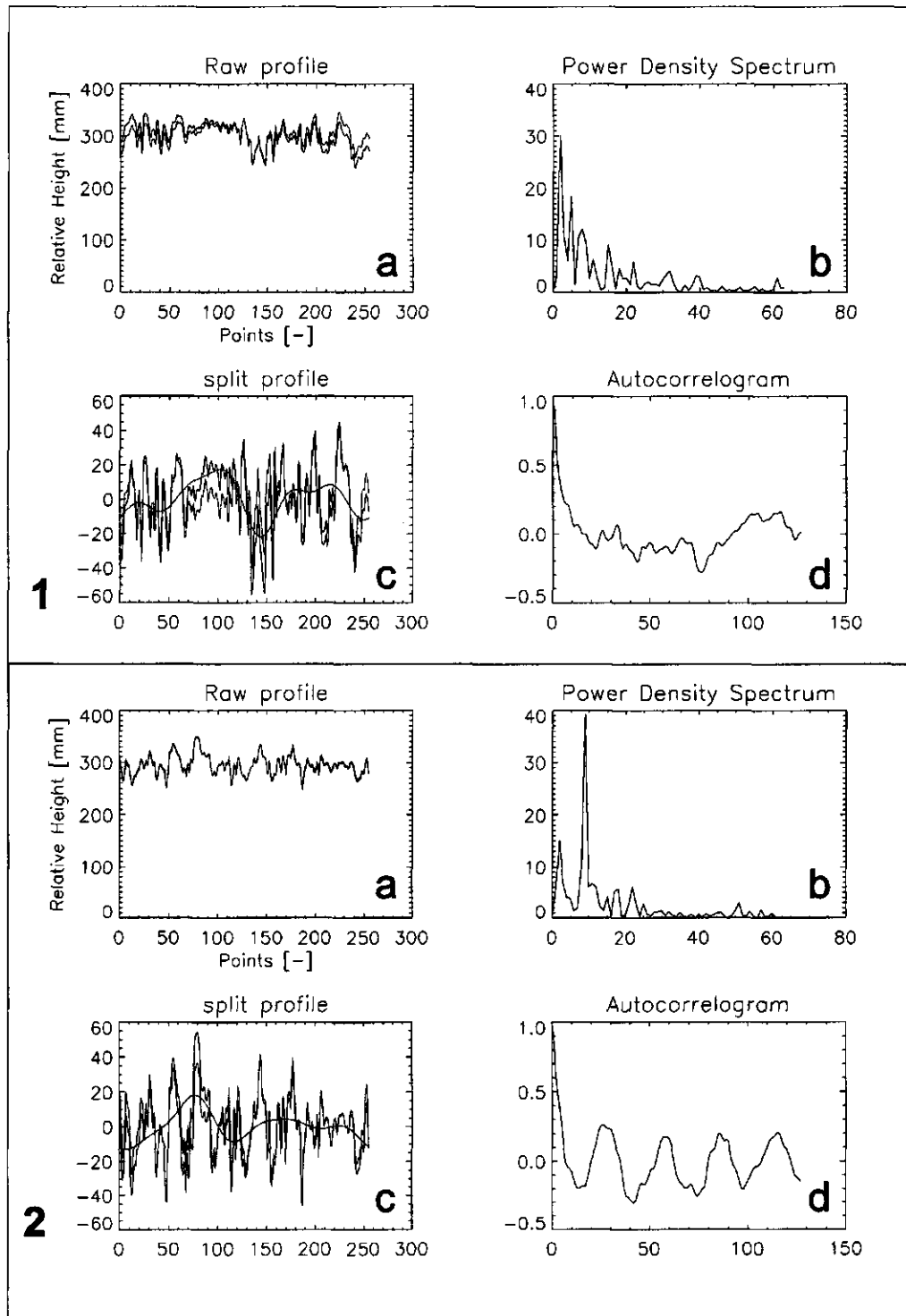of the surface roughness data measurements of 2a and 2b
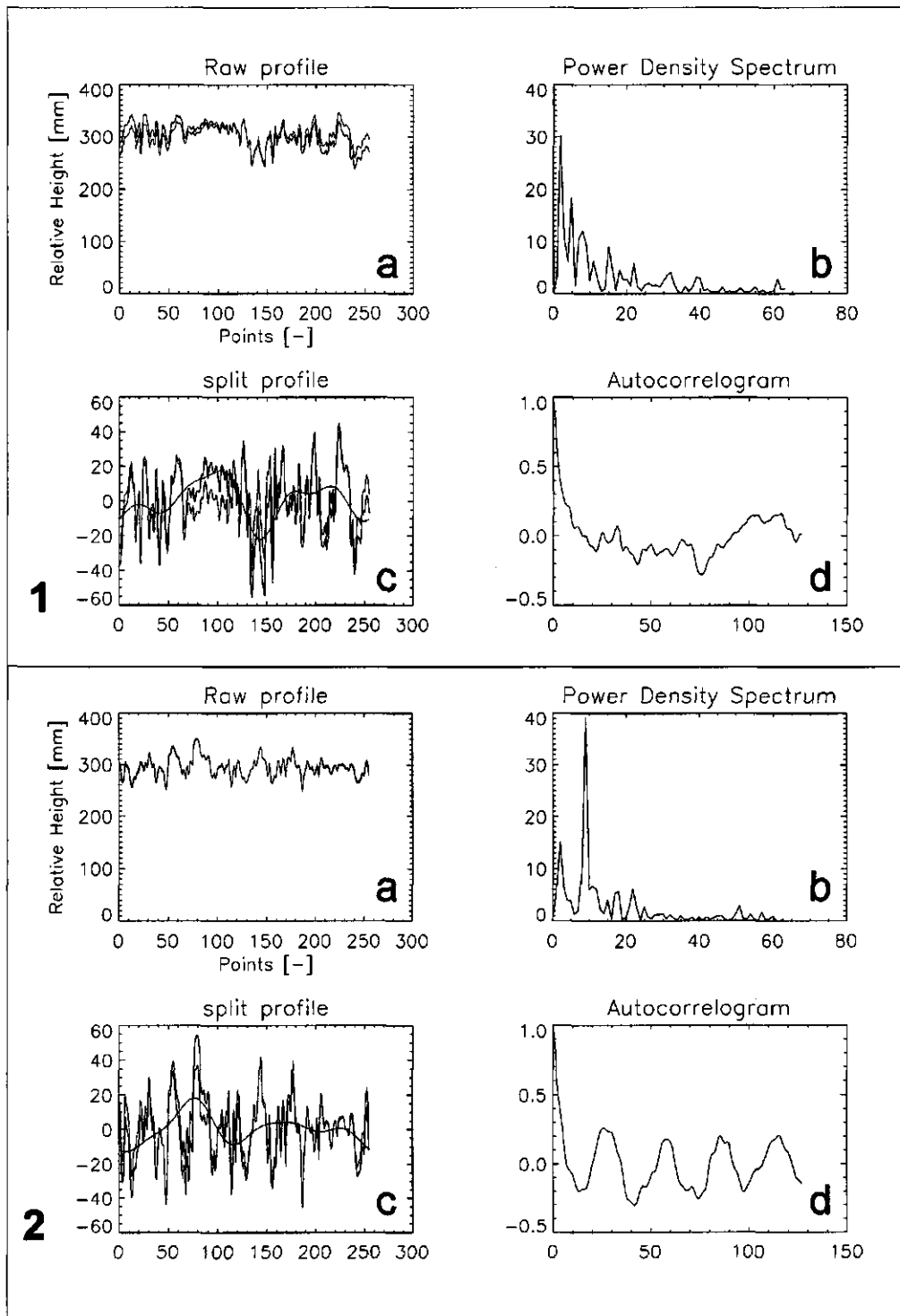
Figure B.4: Raw profile, Power density spectrum, Split profile and Autocorrelogram of the surface roughness data measurements of 2c and 2d

Figure B.5: Raw profile, Power density spectrum, Split profile and Autocorrelogram of the surface roughness data measurements of 2e and 2d

Figure B.6: Raw profile, Power density spectrum, Split profile and Autocorrelogram of the surface roughness data measurements of 2g and 2h
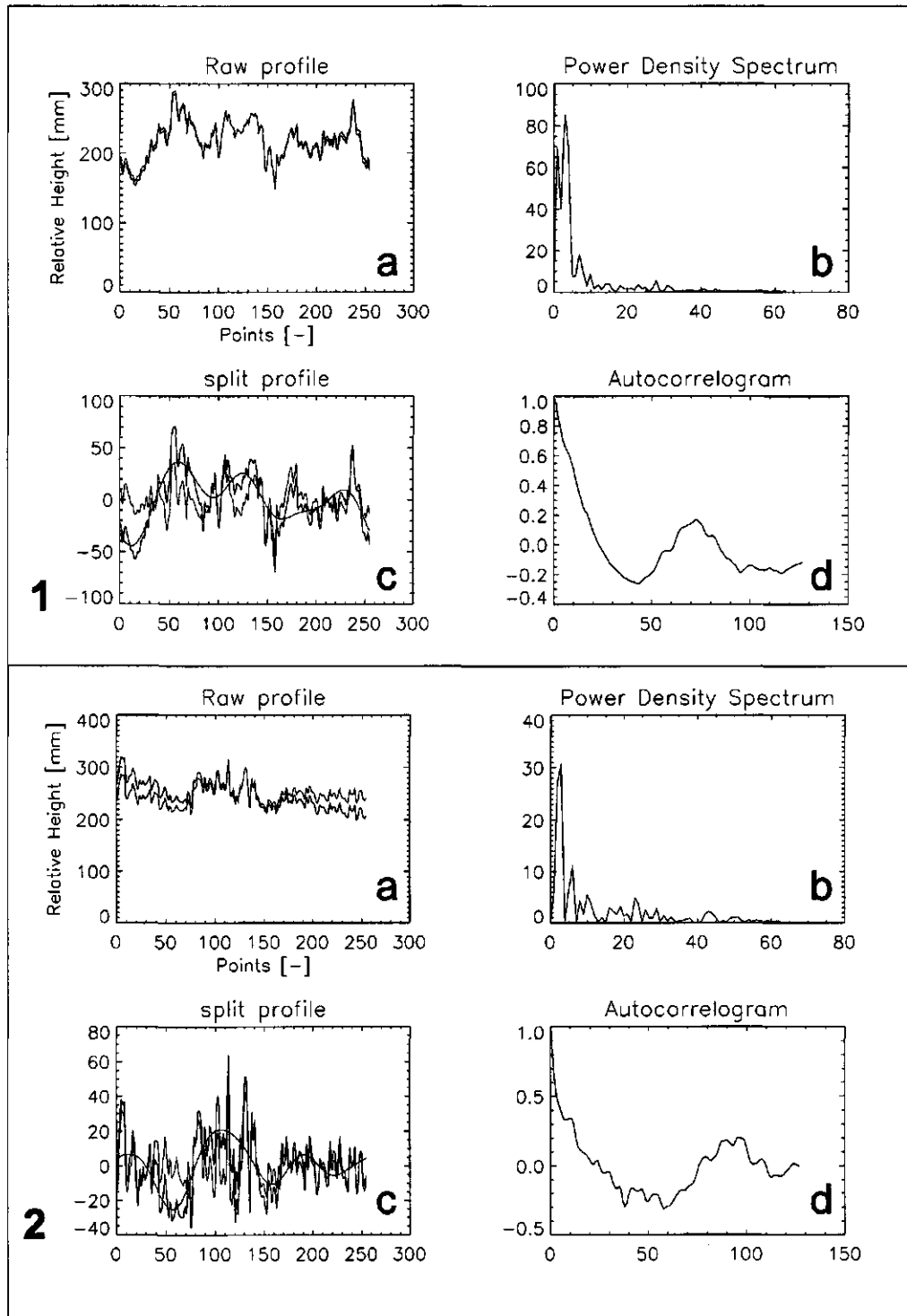
Figure B.7: Raw profile, Power density spectrum, Split profile and Autocorrelogram of the surface roughness data measurements of 3a and 3b

Figure B.8: Raw profile, Power density spectrum, Split profile and Autocorrelogram of the surface roughness data measurements of 3c and 3d

Figure B.9: Raw profile, Power density spectrum, Split profile and Autocorrelogram of the surface roughness data measurements of 4a and 4b
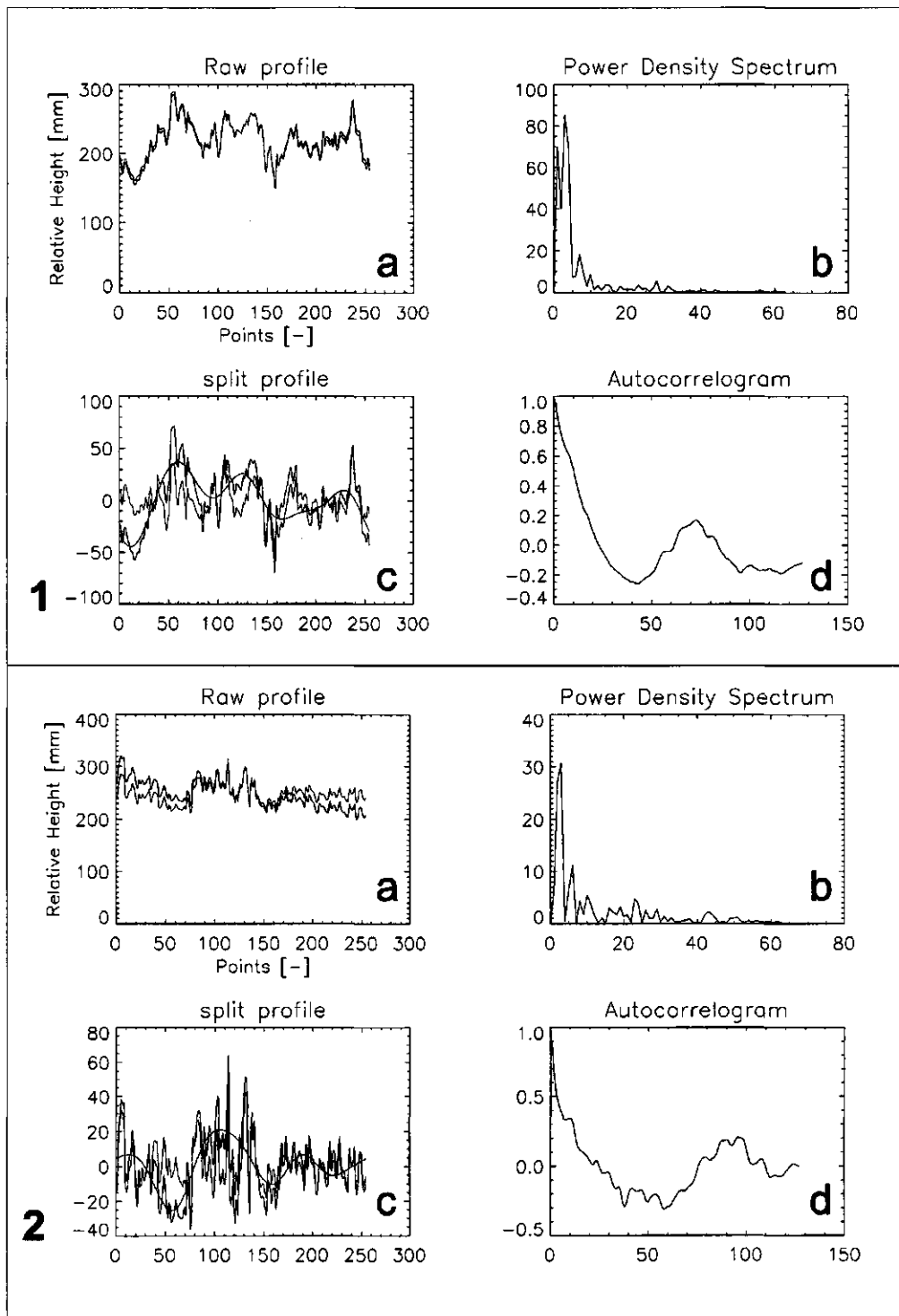
Figure B.10: Raw profile, Power density spectrum, Split profile and Autocorrelogram of the surface roughness data measurements of 4c and 4d
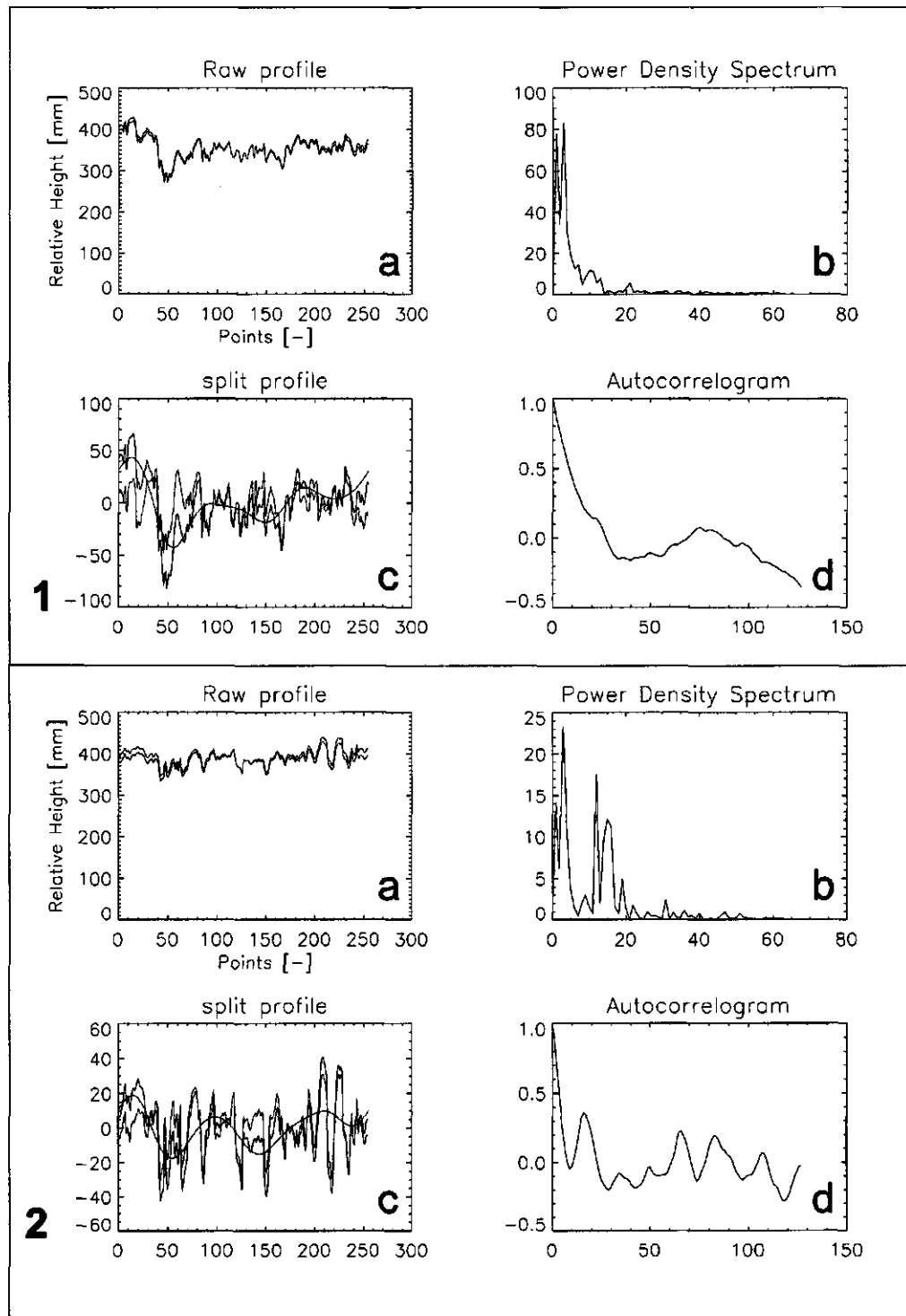
Figure B.11:  Raw profile, Power density spectrum, Split profile and Autocorrelogram of the surface roughness data measurements of 5a and 5b
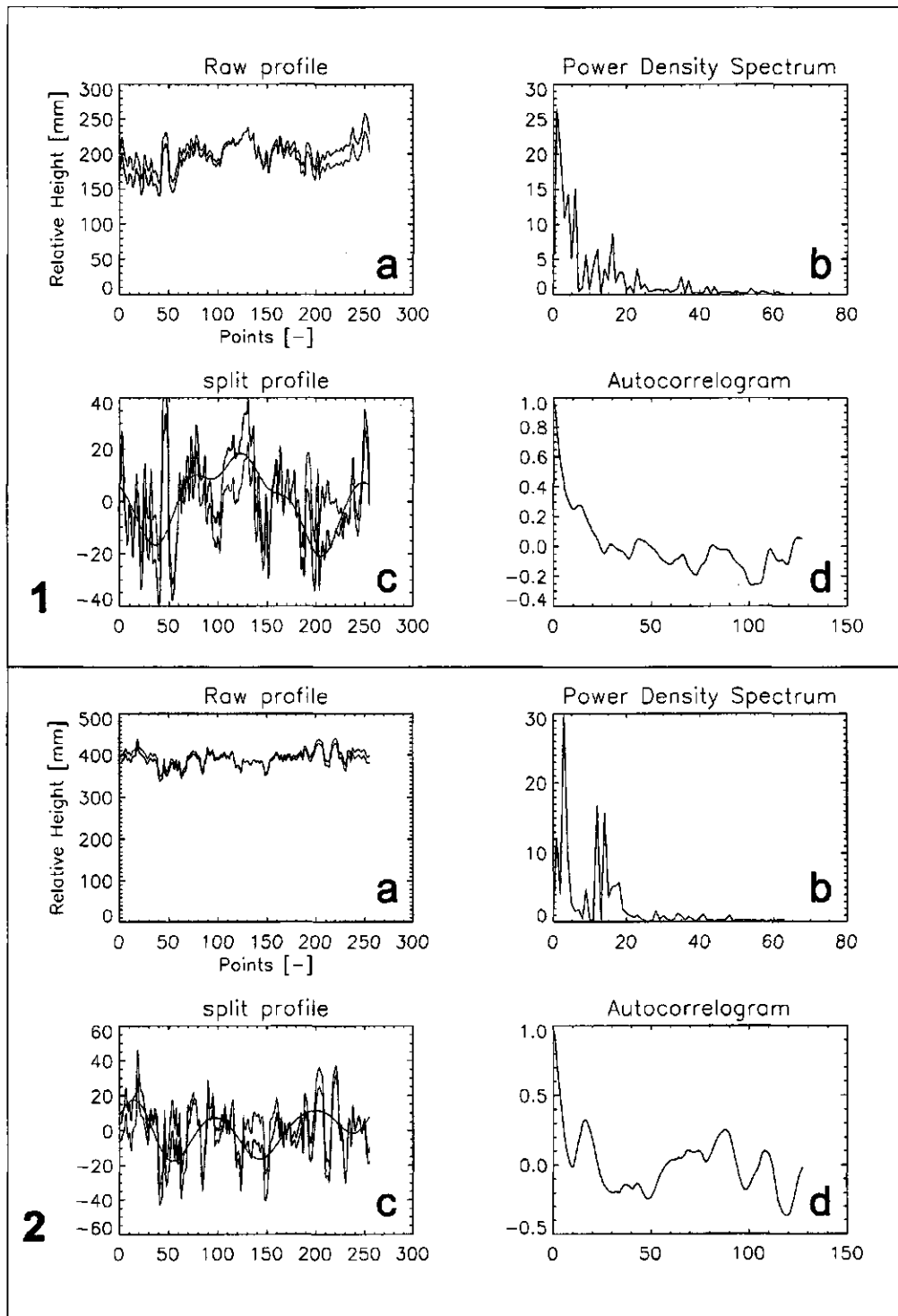
Figure B.12: Raw profile, Power density spectrum, Split profile and Autocorrelogram of the surface roughness data measurements of 5c and 5d
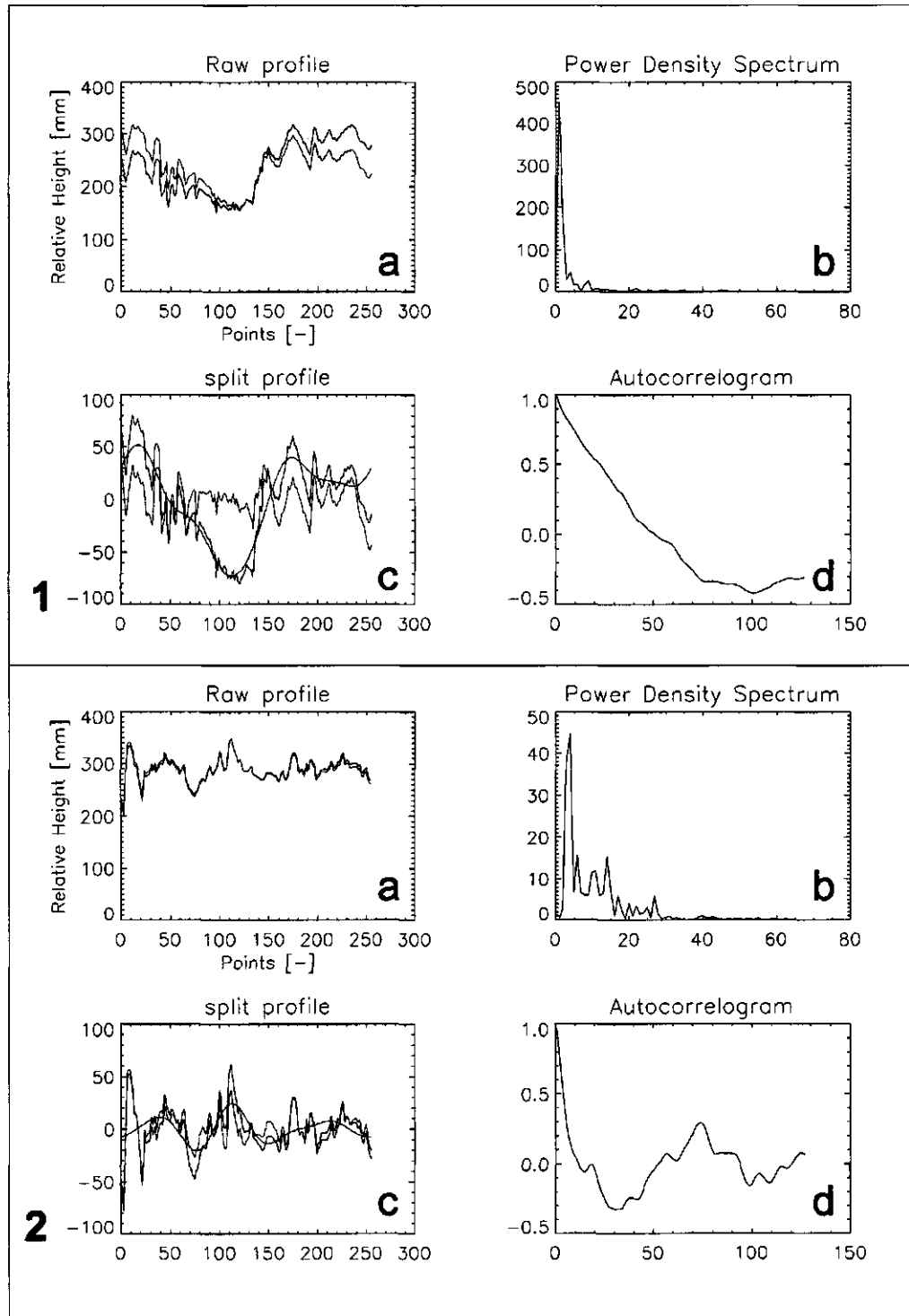
Figure B.13:  Raw profile, Power density spectrum, Split profile and Autocorrelogram of the surface roughness data measurements of 6a and 6b
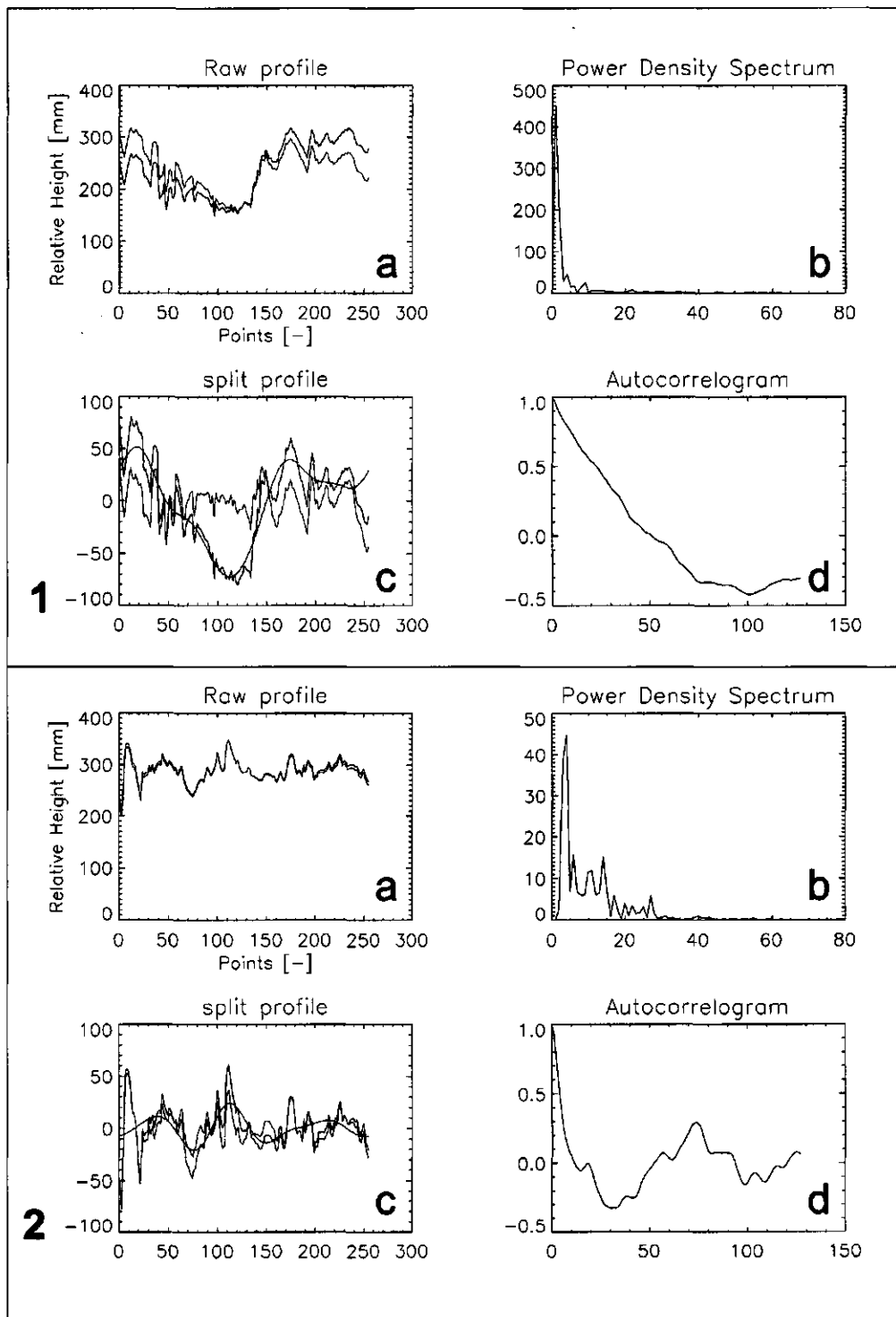
Figure B.14: Raw profile, Power density spectrum, Split profile and Autocorrelogram of the surface roughness data measurements of 6c and 6d
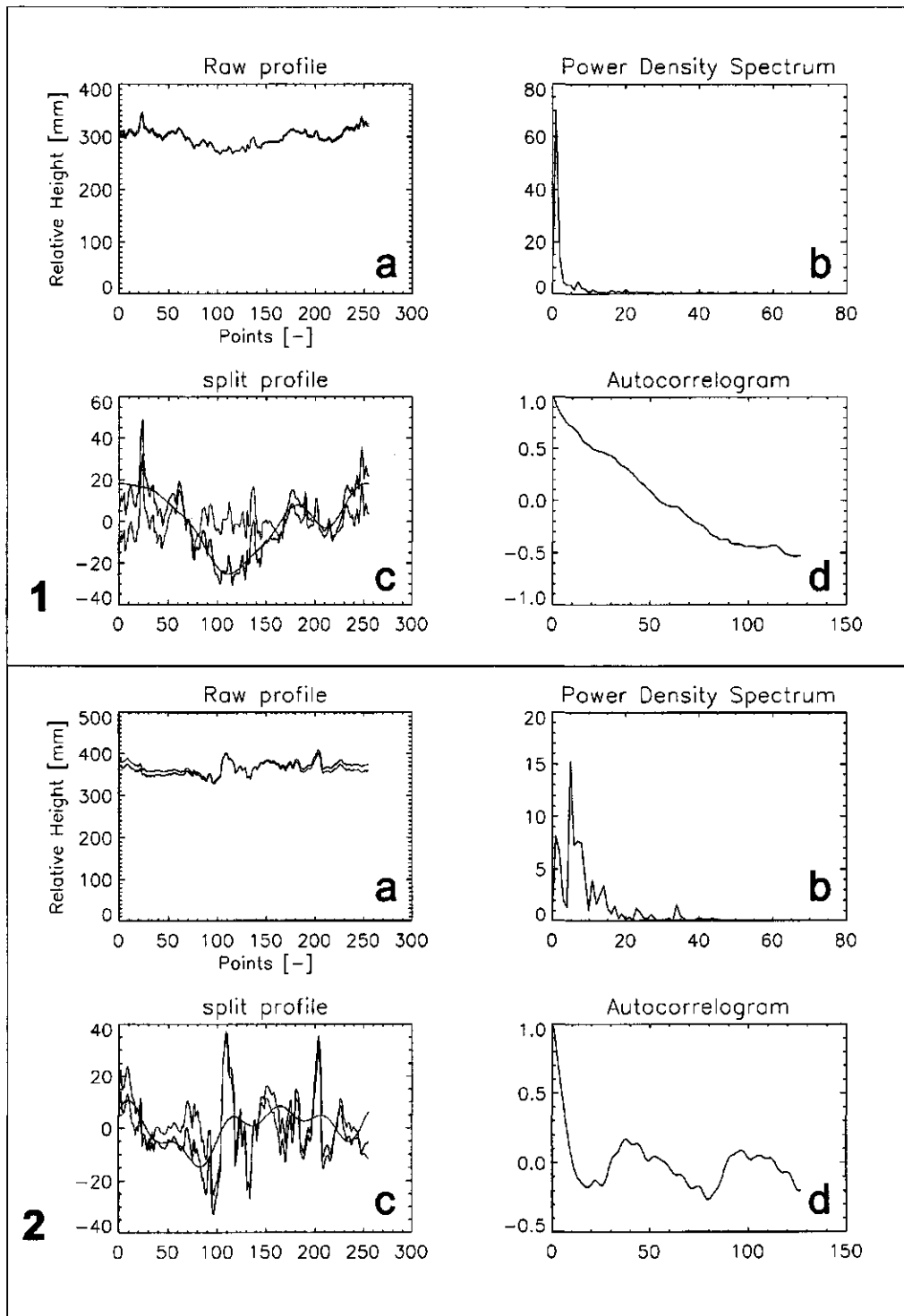
Figure B.15:  Raw profile, Power density spectrum, Split profile and Autocorrelogram of the surface roughness data measurements of 7a and 7b
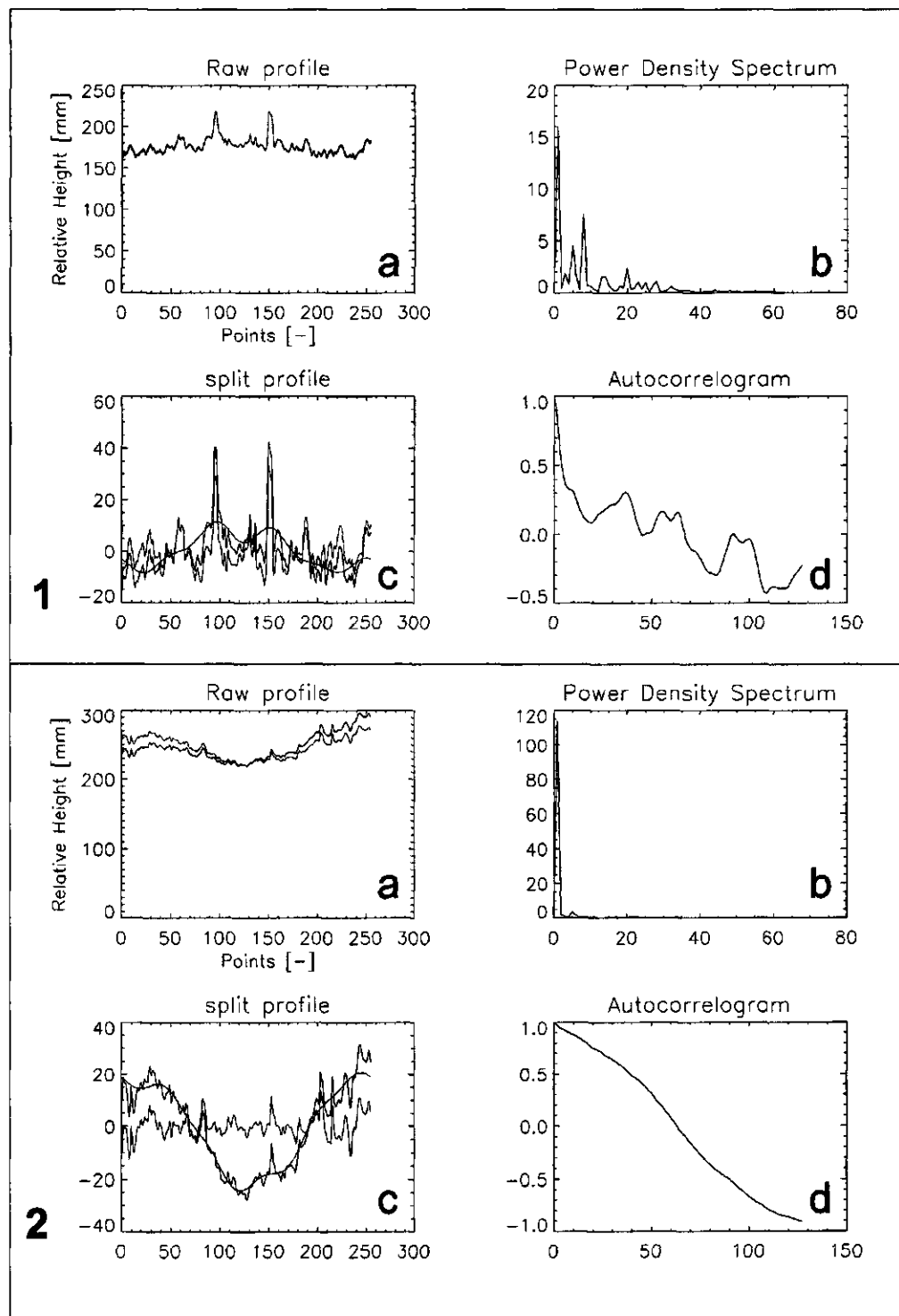
Figure B.16: Raw profile, Power density spectrum, Split profile and Autocorrelogram of the surface roughness data measurements of 7c and 7d

# Appendix C

# Inversion of WSC Data

## C.1 Forward Model

In endeavouring to retrieve geophysical parameters from the WSC data, it is necessary to develop a forward model that accounts for those effects considered important at C-Band VV and which are relevant for the region under observation. In our treatment, the resolution cell is represented by an equivalent surface consisting of a combination of only two surface types: dense, homogeneous vegetation (pure volume scattering) with a fractional surface area denoted by $C$, and bare soil with effective (homogeneous) roughness and dielectric properties (surface scattering). The total backscatter is therefore considered to be an incoherent sum of three backscattering mechanisms: these are (vegetation) volume scattering, surface scattering from the bare soil layer, and specular (double-bounce) reflection between the trunk and ground. In addition, a fourth term may be added which accounts for all other contributions not included in the first three. Since this term may include contributions from such features as highly specular surfaces, its overall effect may be to reduce the total observed backscatter, so that it may be considered to be a random error on the forward model calculation.

Specific models are adopted for each component separately, and their contributions are calculated for an incidence angle $\theta_i$ and azimuth angle $\phi_i$, and are summed incoherently so that

$$\sigma^0(\theta_i, \phi_i) = C\sigma^0_{cover} + [1 - C]\sigma^0_{bare} + \sigma^0_{double} + \sigma^0_{other} \qquad \text{(C.1)}$$

where,

$\sigma^0(\theta_i, \phi_i)$ = scattering coefficient measured at the WSC,

$C$ = equivalent fractional vegetation cover,

$\sigma^0_{cover}$ = contribution from equivalent vegetation cover,

$\sigma^0_{bare}$ = contribution from equivalent bare soil,

$\sigma^0_{double}$ = contribution from double-bounce scattering,

$\sigma^0_{other}$ = contribution from other sources.

The individual contributions may be modelled in a number of different ways, from simple empirical models to elaborate radiative transfer models. The choice is dependant upon the specific problem at hand, and is influenced by such factors as the availability and reliability of ground truth, or the parameters one wishes to determine from the measurements. In the current study, the nature of the investigation is to monitor an area with limited ground data and with a high degree of variation in surface parameters. A simple approach is therefore adopted in order to illustrate

the applicability of this method, and to highlight the potential of using WSC data. In the current study, $\sigma^0_{cover}$ was kept constant (such that $\sigma^0_{cover}/\cos\theta_i = -6.0$) and

$$\sigma^0_{bare} = \frac{|R_g|^2}{2s^2\cos^4\theta_i}\exp(-\tan^2\theta_i/2s^2) \tag{C.2}$$

$$\sigma^0_{double} = T R_1 R_2 \sin^2(\theta_i + 45°). \tag{C.3}$$

## C.2   WSC Inverse Model

In many physical problems the forward model can be expressed in the simplified linear quadrature form

$$\mathbf{y} = \mathbf{Kx} + \boldsymbol{\epsilon}_y \tag{C.4}$$

where the elements of the vector $\boldsymbol{\epsilon}_y$ represent the error or noise associated with each measurement $y_i$ and $\mathbf{K}$ now represents the forward model (Equation C.1) as a kernel matrix which characterises the measurements made by the instrument (represented by the vector $\mathbf{y}$) and describes how they depend on the state of the illuminated surface region (represented by the vector $\mathbf{x}$). In the problem at hand, the surface state vector is defined as

$$\mathbf{x} = \begin{bmatrix} C \\ s \\ T \\ |R_g|^2 \end{bmatrix}$$

The retrieval, or inverse, problem then requires deducing the best estimate of the state $\mathbf{x}$ of the observed ground area from a set of measurements $\mathbf{y}$. In the case of the WSC, there are only three measurements to determine four parameters, so that a priori information is required to constrain the solution.

A common approach to the inverse problem is to assume that all the statistical distributions within the problem are Gaussian so that an Optimal Estimation (or Maximum Likelihood) method may be employed (Rodgers, 1976). Such a method allows for the use of the *a priori* information to constrain the final solution and gives the optimum solution $\hat{\mathbf{x}}$ as

$$\hat{\mathbf{x}} = \mathbf{x}^{(0)} + \mathbf{S}_x\mathbf{K}^T(\mathbf{KS}_x\mathbf{K}^T + \mathbf{S}_\epsilon)^{-1}(\mathbf{y} - \mathbf{y}^{(0)}) \tag{C.5}$$

where, $\mathbf{x}^{(0)}$ represents the *a priori* state vector with its associated error covariance matrix $\mathbf{S}_x$, $\mathbf{S}_\epsilon$ is a diagonal measurement error covariance matrix, with elements equal to $\boldsymbol{\epsilon}_y$, and $\mathbf{y}^{(0)} = \mathbf{Kx}^{(0)}$.

An alternative interpretation is to consider the *a priori* information as a *virtual measurement* with mean $\mathbf{x}^{(0)}$ and error covariance $\mathbf{S}_x$. The normal rules for combining measurements (Houghton, 1977; Rodgers, 1976) then give Equation C.5 directly. The covariance $\hat{\mathbf{S}}$ of the estimate $\hat{\mathbf{x}}$ is then

$$\hat{\mathbf{S}} = \mathbf{S}_x - \mathbf{S}_x\mathbf{K}^T(\mathbf{KS}_x\mathbf{K}^T + \mathbf{S}_\epsilon)^{-1}\mathbf{KS}_x \tag{C.6}$$

The diagonal of the solution covariance matrix contains the variances, or squares of standard deviations, of the individual components of the solution $\hat{\mathbf{x}}$ and thus gives a measure of accuracy of the solution.